



HAL
open science

Possibly seismically triggered avalanches after the S1222a Marsquake and S1000a impact event

A. Lucas, I.J. Daubar, M. Le Teuff, Clement Perrin, T. Kawamura, L. Posiolova, P. Lognonné, S. Rodriguez, D. Giardini, G. Sainton, et al.

► **To cite this version:**

A. Lucas, I.J. Daubar, M. Le Teuff, Clement Perrin, T. Kawamura, et al.. Possibly seismically triggered avalanches after the S1222a Marsquake and S1000a impact event. *Icarus*, 2024, 411, pp.115942. 10.1016/j.icarus.2023.115942 . hal-04386179

HAL Id: hal-04386179

<https://hal.science/hal-04386179>

Submitted on 10 Jan 2024

HAL is a multi-disciplinary open access archive for the deposit and dissemination of scientific research documents, whether they are published or not. The documents may come from teaching and research institutions in France or abroad, or from public or private research centers.

L'archive ouverte pluridisciplinaire **HAL**, est destinée au dépôt et à la diffusion de documents scientifiques de niveau recherche, publiés ou non, émanant des établissements d'enseignement et de recherche français ou étrangers, des laboratoires publics ou privés.



Distributed under a Creative Commons Attribution - NonCommercial - NoDerivatives 4.0 International License

Possibly seismically triggered avalanches after the S1222a Marsquake and S1000a impact event

Lucas A.¹, Daubar I. J.², Le Teuff M.¹, Perrin C.³, Kawamura T.¹, Posiolova L.⁴, Lognonné P.¹, Rodriguez S.¹, Giardini D.⁵, Sainton G.¹, Mangeney A.¹, McEwen A.⁶

¹Université Paris Cité, Institut de physique du globe de Paris, CNRS, F-75005, Paris, France

²Brown University, Providence, RI, USA

³Nantes Université, Université d'Angers, Le Mans Université, CNRS, UMR 6112, Laboratoire de Planétologie et

Géosciences, UAR 3281, Observatoire des Sciences de l'Univers de Nantes Atlantique, Nantes, France

⁴Malin Space Science System, San Diego, CA, USA

⁵ETH, Zurich, Switzerland

⁶U. Arizona, USA

Key Points:

- On May 4, 2022, a major martian seismic event was recorded
- We identified possibly seismically induced dust avalanches in the area of the estimated epicenter
- We discuss avalanche triggering conditions and derive a possible epicenter location based on avalanche spatial density

Corresponding author: A. Lucas, lucas@ipgp.fr

Abstract

Ground motion from seismic events detected by the SEIS/InSight seismometer on Mars could potentially trigger dust avalanches. Our research strongly suggests that the seismic event S1000a may have triggered a significant number of dust avalanches. In contrast, following the seismic event S1222a, there was only a modest increase in avalanche occurrences. Orbital observations of the area surrounding the projected location of the S1222a quake reveal notable topographic features, such as North-South ridges and impact craters. We utilize orbital imagery to evaluate the rate of avalanches and explore how the S1222a event might have influenced this rate. The S1222a event appears to be a plausible factor contributing to the observed increase in avalanches. Our further analysis of the epicenter location aims to clarify how it aligns with the avalanches' spatial distribution, offering insights into the regional topography.

Plain Language Summary

We explore the potential effects of seismic aftermath on Mars, focusing on how large seismic events might trigger dust avalanches and mass wasting. Our analysis of orbital data reveals that the affected area is characterized by steep slopes, predominantly around crater walls, where dust accumulation is substantial. This geological setup makes the region particularly prone to dust avalanches. Large seismic events are known to cause ground acceleration, which can reduce material cohesion and friction, or increase tangential strain. These changes are conducive to mass wasting. Based on our research, we propose that the S1222a marsquake could be a primary factor contributing to the observed increase in avalanche activity, as evidenced by our analysis of orbital imagery. This finding sheds light on the dynamic interplay between seismic activity and surface processes on Mars.

1 Introduction

On May 4, 2022, a major seismic event named S1222a (Kawamura et al., 2023) was recorded by the SEIS instrument (Lognonné et al., 2019) of the InSight mission (Banerdt et al., 2020). It was an unprecedented marsquake in the SEIS recording period with an estimated moment magnitude of M_W^{Ma} 4.7 (InSight Marsquake Service, 2022). In comparison, 95% of events recorded by SEIS since landing in November 2018 had a magnitude below 3.5 (Clinton et al., 2021; Böse et al., 2021; Ceylan et al., 2022; Knapmeyer et al., 2023). As for some of the InSight events, a location was estimated with a back-Azimuth (bearing from the event toward InSight) of 101° (96° - 112°) and an epicentral distance $\Delta = 37^\circ$ ($\pm 1.6^\circ$) which places the event epicenter at the location of 3.0° S, 171.9° E (Kawamura et al., 2023) (green star on Fig. 1). Other nearby locations for the epicenter have also been proposed (Panning et al., 2023; Kim et al., 2022) (Fig. 1). No new impact crater has been reported that could be the source of this event (Fernando et al., 2023). The region shows many topographic features including a few tectonic structures expressed as north-south wrinkle ridges (Knapmeyer et al., 2006) and impact craters (Fig. 1). To the east of this region, the only major structures are Appollinaris Patera, a Noachian volcano (Tanaka et al., 2014) about 200 km in diameter, and a large alluvial fan spanning southwards from the volcano's rim.

From orbital images, we identified dust avalanches (also known as slope streaks) in this region (orange symbols on Fig. 1). These are known active mass wasting processes occurring on Mars in several contexts (Ferguson & Lucchitta, 1984; Sullivan et al., 2001; Aharonson et al., 2003; Schorghofer et al., 2002, 2007; Schorghofer & King, 2011; Gerstell et al., 2004; Baratoux et al., 2006; Chuang et al., 2007; Bergonio et al., 2013; Heyer et al., 2019, 2020; Valantinas et al., 2021). They appear as relatively dark or bright streaks on steep dust-covered slopes and occur in regions with a high albedo and low to very low thermal inertia (Sullivan et al., 2001; Aharonson et al., 2003). Dust avalanches on Mars typically appear darker than the surrounding terrain. This is likely due to the removal of lighter-colored surface dust by the avalanches. When a slope streak is formed, loose dust and sand on the

68 surface are mobilized and cascade down the slope, exposing the darker, underlying material
 69 (Malin et al., 2007; Dundas, 2020). This material may be darker due to several factors, such
 70 as the presence of iron-rich minerals or alteration by weathering processes (Christensen et
 71 al., 2001). In addition, the removal of surface dust by the avalanches may expose a rougher,
 72 more textured surface, which can scatter and absorb more light, making the streak appear
 73 even darker. Many studies discuss possible triggering conditions and emplacement mecha-
 74 nisms. Purely dry avalanches of fine dust have been explored from the perspective of both
 75 observations (Schorghofer et al., 2007; Phillips et al., 2007; Dundas, 2020), and numerical
 76 simulations (Lucas, 2010). Spring discharge involving salty groundwater and/or brines in
 77 the shallow subsurface has been proposed (Ferris et al., 2002; Miyamoto, 2004; Head et al.,
 78 2007; Kreslavsky & Head, 2009; Bhardwaj et al., 2017, 2019). Other possible triggers in-
 79 clude wind (Baratoux et al., 2006; Heyer et al., 2019), seismic activity from impacts or inter-
 80 nal forces, or boulder track (Chuang et al., 2007) have been proposed.

81 While previous studies looked at boulder falls and associated tracks triggered by possi-
 82 ble paleo-seismic activity (Roberts et al., 2012; Brown & Roberts, 2019), no previous work
 83 could have directly tested the possibility of seismically induced mass wasting on Mars due
 84 to a lack of seismic event records before the InSight mission. In the framework of the recent
 85 seismic events S1000a and S1222a, we investigate the effects of the induced ground accelera-
 86 tion aftermaths as a potential triggering mechanism for dust avalanches in the vicinity of the
 87 located epicenter. To do so, we conduct regional mapping of the avalanches from pre-event
 88 and post-event imagery in order to estimate the effect of the marsquake and impact crater on
 89 the rate of avalanches. We take into account possible biases due to the limited number of im-
 90 ages, the time span between images, the sub-surface properties through thermal behavior,
 91 and the various sensitivities of each camera sensor.

92 2 Methods

93 2.1 Orbital data and mapping

94 As soon as the S1222a event was detected by SEIS and an estimate of the epicenter
 95 location was provided, we investigated orbital observations provided by the Context (CTX)
 96 and High Resolution Imaging Science Experiment (HiRISE) cameras (Malin et al., 2007;
 97 McEwen et al., 2007), both on board the Mars Reconnaissance Orbiter (MRO). Along with
 98 MRO imagery, we examine images from the Mars Global Surveyor (MGS)/Mars Orbiter
 99 Camera (MOC) (Malin et al., 1992), and THEMIS-Vis/Odyssey (Fergason et al., 2006).
 100 This led to a set of hundreds of images acquired before the seismic event. In addition, we
 101 requested new MRO observation over areas where we mapped avalanches inside the un-
 102 certainty area (Kawamura et al., 2023) (Fig. 1, Supp. Info text S1). At the time of writing
 103 this paper, a dozen HiRISE images and thirty new CTX observations were obtained, all ac-
 104 quired after the S1222a seismic event. In addition to imagery, we used Digital Terrain Mod-
 105 els (DTMs) from both Mars Orbiter Laser Altimeter (MOLA, Smith et al. (2001)) and High
 106 Resolution Stereo Camera (HRSC, Neukum and Jaumann (2004)), the geological map from
 107 Tanaka et al. (2014) and the thermal inertia map (Christensen et al., 2004) (See Supp. Info.
 108 Text S2), which all provide contextual information. Note that Figure 1 specifically depicts
 109 the area covered by post-S1222a event CTX imagery. All the data have been combined into
 110 a Geographical Information System (GIS) in order to manually map all avalanches in the re-
 111 gion of interest (Fig. 1), by two independent people (see Supp. Info. Text S1 for details on
 112 the imagery processing and mapping). The older observations, provided by both MOC and
 113 THEMIS-Vis, were only used for confirming the very low fading rate (Sullivan et al., 2001),
 114 being in good agreement with the dust activity reported in this region (Battalio & Wang,
 115 2021).

116 2.2 Estimates of avalanche rate and statistics

117 Avalanche rate q is obtained from equation provided in Aharonson et al. (2003):

$$q = 100 \times \frac{\Delta n}{n\Delta t}, \quad (1)$$

118 where n is the total number of avalanches observed in both the two overlapping im-
 119 ages, Δn being the newly observed avalanches on the recent image and not in the older im-
 120 age, and Δt being the time span between the two observations in Martian years. This rate q
 121 is expressed in % of new events/Martian year (Aharonson et al., 2003). This method has also
 122 been used by recent work (Heyer et al., 2019). The time periods between overlapping images
 123 in our database range from ~ 0.3 to almost 7 martian years.

124 Finally we agglomerate avalanches in the same location (i.e. crater) and hence to com-
 125 pute the avalanche rate in each area where new events can be observed between two over-
 126 lapping images. As opposed to a squared binning, hexagons are more similar to circles,
 127 hence they better translate data aggregation around the bin center. As most areas covered
 128 by avalanches in this region are impact craters, this provides a more valuable way to decipher
 129 the avalanche coverage.

130 3 Results and discussion

131 3.1 Avalanches triggered after S1000a impact event

132 Before discussing S1222a event, we investigated S1000a impact event which occurred
 133 on September 18 2021, and left a crater over 150 m in diameter at $38.1^\circ\text{N}; -79.87^\circ\text{E}$ (Fig. 2).
 134 This event was recorded by SEIS and then orbital imagery revealed its actual location. Its
 135 magnitude was estimated to be around M_w^{Ma} 4.1, hence about 25 times smaller than S1222a
 136 in energy (Ceylan et al., 2022; Posiolova et al., 2022). It should be noted that the location
 137 estimate from the seismic signal analysis was felt at approximately 130 km away from the
 138 actual location, as discussed in (Posiolova et al., 2022). By analysing all pre-event images
 139 including CTX, and HRSC and post-event HiRISE images, we could map a very large num-
 140 ber of avalanches not seen in pre-event imagery. By looking back in time using all avail-
 141 able images, including MOC/MGS, we observed that these areas were not covered by dust
 142 avalanches prior to the impact event (Fig. 2.).

143 We looked at the the density distribution of the new avalanches (as seen on the post-
 144 event images and having the same brightness, hence the same age) as a function of their re-
 145 spective distance to the impact crater (histogram inset in Fig. 2). This distribution follows
 146 a bell-shaped curve. As seen on Earth, seismically triggered mass-wasting is absent very
 147 close to the epicenter, and increases at farther distances until it decreases again at the farthest
 148 distances (e.g., Tatard, 2010; Livio & Ferrario, 2020). Nonetheless, the mechanism here is
 149 different. It is very likely that the avalanches are triggered by secondary impacts, and not
 150 seismic waves. As an example of a typical scenario, ejecta leaving the primary impact at a
 151 velocity $v = 200 \text{ m}\cdot\text{s}^{-1}$, with a launch angle of $\theta = 45^\circ$, will have a ballistic flight time t_f of
 152 76 sec (i.e., $t_f = 2 \times v \sin \theta / g$), and will land at a distance $d_l = 10.78 \text{ km}$ (neglecting the air
 153 friction, $d_l = v \cos \theta \times t_f$). Hence, the histogram in the inset of figure 2 is similar to the statis-
 154 tical distribution of secondary ejecta impacting the ground. This correlation indicates those
 155 secondary impacts are a likely source for the avalanches. Of course, the S1000a event is an
 156 ideal case. First of all, we know the position of the epicenter perfectly well, thanks to the or-
 157 bital imagery revealing the source crater. What's more, the presence of northeast-southwest
 158 trending ripples implies the presence of uniformly distributed topographic slopes as mov-
 159 ing away from the impact crater, hence the avalanche susceptibility. Note that Burleigh et
 160 al. (2012) demonstrated that impact blast can trigger slope streaks. The S1000a event also
 161 shows that an impact with a seismic magnitude M_w^{Ma} 4.1 can trigger a very large number of
 162 avalanches on Mars. As such, this is likely to be discussed more thoroughly in a following work
 163 which would evaluate the ballistic recomposition in order to evaluate potential effects of sec-
 164 ondary impacts on the dust avalanche triggering. However, the ground accelerations caused

165 by a surface impact and a deep earthquake are not the same. So, in view of our results for the
 166 S1000a event, we discuss our results for S1222a in the following sections.

167 3.2 Avalanche rate increase in post-marsquake S1222a images

168 We analyzed all image pairs over the whole area of interest near the S1222a estimated
 169 epicenter. We identified 4532 avalanches (orange symbols in Figure 1). More than 200 avalanches
 170 were identified on pre-event images (over the 2005–2021 period), and 122 were identified on
 171 the post-event CTX images with respect to their 2005–2021 period counterparts respectively.
 172 An example is given in Figure 3-a. Note that, while doubtful avalanches may have been de-
 173 tected (e.g., yellow symbols in Fig. 3-a), we only took into account the robust observations
 174 of new avalanches (e.g., red symbols in Fig. 3-a). For the statistical robustness, we then de-
 175 rived avalanche rates q for each CTX/CTX pair only. When times series were available, we
 176 derived avalanche rate chronicles (Fig. 3-b). As exemplified on Fig. 3-b, a strong increase
 177 of q is observed after the S1222a event. Indeed, over the whole area of interest (Fig. 1),
 178 the pre-event rates (circles in fig. 3-c) lie around $2.6\%.\text{MYear}^{-1}$ with a maximum value of
 179 $6\%.\text{MYear}^{-1}$, accounting for uncertainties following Aharonson et al. (2003). These values
 180 are in agreement with in previous estimated by Aharonson et al. (2003), and avalanche rates
 181 do not differ substantially across the region covered by our study. In contrast, post-event val-
 182 ues of q show a significantly different distribution both spatially and in amplitude (Figure 3-
 183 c,d). While most rates still fall below 10%, we observe that in 9 places, the rates are $>10\%$,
 184 as high as 40% (excluding outlier, Figure 3-d). If we keep only the sub-10% values, the aver-
 185 age is the same as that before the seismic event ($2.6\%.\text{MYear}^{-1}$), and there is also no depen-
 186 dence on the epicentral distance. Interestingly, the highest post-event q ($>20\%$) are found at
 187 the smallest distances from the epicenter of the S1222a event proposed by Kawamura et al.
 188 (2023). When relating the derived avalanche rate q to the epicentral distance Δ with respect
 189 to the estimated location from Kawamura et al. (2023), we obtained a slight decreasing trend
 190 of q with Δ . Finally we also verified that temporal sampling of the orbital images (Δt) does
 191 not bias the avalanche rate estimates (Fig. 3-e).

192 To address the limited number of observations, we employed a permutation test, also
 193 known as bootstrapping (Efron & Tibshirani, 1993; Davison & Hinkley, 1997). This non-
 194 parametric approach does not rely on specific distribution assumptions about the data. We
 195 began by calculating the avalanche rate for each CTX/CTX pair for both pre-event and post-
 196 event observations, determining the mean difference as our observed statistic. Then, we
 197 merged the pre-event and post-event rates, treating them as a combined dataset without dis-
 198 tinction of their original times. This pooled data was randomly shuffled to create new groups,
 199 preserving the original group sizes. We calculated the permuted test statistic by assessing the
 200 avalanche rate in this permuted data. This permutation process was iterated a million times,
 201 generating a distribution of test statistics under the hypothesis of no marsquake influence.
 202 Comparing our observed statistic to the 95% confidence interval derived from bootstrap-
 203 ping, we found that the post-event avalanche rates in all CTX observations exceeded 95% of
 204 the bootstrap statistic distribution. This indicates a significant increase in avalanche activity
 205 following the seismic event. However, it is important to note that the area studied includes
 206 locations possibly too distant from the epicenter to be affected by the marsquake. Focusing
 207 on rates exceeding $6\%.\text{MYear}^{-1}$, the post-marsquake rates surpassed the 99.98% confidence
 208 level. These findings, along with the detailed bootstrapping procedure, are outlined in Algo-
 209 rithm 1 and illustrated in Figure 4.

210 3.3 Effect of the relative thermal inertia

211 Subsurface properties at shallow depths can be analyzed through thermal inertia, which
 212 indicates how solar energy absorption and subsequent subsurface heat propagation relate
 213 to material properties. Thermal inertia is represented as $\Gamma \equiv \sqrt{\kappa_e(1-p)\rho C(T)}$, where κ_e
 214 denotes effective thermal conductivity, p is porosity, ρ represents density, and $C(T)$ is the
 215 specific heat capacity. Therefore, low thermal inertia can indicate high porosity, low den-

Algorithm 1: Assessing Influence of marsquake on avalanche rate**Input:** Pre-event image pairs $(n, \Delta n, \Delta t)$ **Input:** Post-event image pairs $(n, \Delta n, \Delta t)$ Define the observed test statistic: Δn_{obs} (change in the number of avalanches), n_{obs} (number of avalanches), and Δt_{obs} (time difference between images);

Combine the before and after data into a single pool, disregarding their original labels;

Perform resampling with replacement: Randomly sample, with replacement, from the pooled data to create a bootstrap sample of the same size as the original data set. Repeat this process to generate a large number of bootstrap samples.

Calculate the test statistic for each bootstrap sample: Compute the rate of avalanches for each bootstrap sample, given by $\frac{\Delta n_{boot}}{n_{boot} \Delta t_{boot}}$;

Calculate the bootstrap statistic distribution: Collect the calculated test statistics from step 4 to form the bootstrap distribution of the test statistic;

Calculate the confidence interval: Determine the desired confidence level (e.g., 95%).

Compute the lower and upper percentiles of the bootstrap distribution corresponding to the chosen confidence level;

Output: Assessment of marsquake influence

sity, small grain size, or a combination of these factors. As Sullivan et al. (2001); Aharonson et al. (2003) previously demonstrated, dust avalanches on Mars typically occur on steep slopes and are found in areas with low absolute thermal inertia. It's important to note that thermal inertia values are derived from models and assumptions, as detailed by Christensen et al. (2004). Due to significant variations between orbits, we calculate the ratio of the apparent value of thermal inertia at avalanche scar location with respect to the median value on the surrounding plains, and named hereafter $\Gamma^* = \Gamma_{avalanche} / \Gamma_{plain}$ (see Supp. Info. Text S2). By examining Γ^* , we found that areas with the lowest values experience the most significant increases in avalanche rates (see Fig. 3-c). Specifically, when $\Gamma^* \gg 1.5$, post-event avalanche rates do not exceed pre-event rates. Conversely, an increase in q is observed when $\Gamma^* < 1.5$. This leads us to conclude that post-event avalanche susceptibility on Mars is primarily influenced by scarp locations with steep slopes and the lowest apparent thermal inertia. Such conditions correspond to the most unconsolidated terrains or areas with fine granular material.

3.4 Epicentral distance and possible sources of the quake

Although the epicentral distance is far from being the only parameter that controls the avalanche rates, it remains an important control factor (Tatard, 2010; Livio & Ferrario, 2020) (Supp. Info. Text S3 and S5). The reason is that the transition between a static state and a flowing state is modelled by introducing a threshold allowing the material to flow. This has been shown to quantitatively capture debris and rock avalanche morphodynamics on Mars (Lucas, 2010; Lucas & Mangeney, 2007; Lucas et al., 2011, 2014) (see Supp. Info. Text S3). Nonetheless, local geology, fractures, aftershocks and historical events will have a significant effect on the aftermaths of an earthquake by leading the slopes close to failure (Tatard, 2010; Livio & Ferrario, 2020; Chen et al., 2020; Rosser et al., 2021; Lombardo & Tanyas, 2022). Taking into account all these considerations, the rate would not be expected to be controlled only by epicentral distance. However, our constraints on the characteristics of the marsquake are weak, especially in terms of depth, focal mechanisms, and therefore the resulting ground acceleration. Our knowledge on the geological heterogeneity is also poorly constrained. Also, compared to terrestrial standards, this marsquake remains a small event. Nonetheless, small seismic events have shown to significantly increase the rate of landslides

246 on Earth (Martino et al., 2022). Indeed, recent studies show that even very small amplitude
 247 seismicity may trigger instabilities on metastable slopes (Bontemps et al., 2020; Durand et
 248 al., Minor revision).

249 Nonetheless, under the hypothesis that event S1222a did trigger avalanches, we consid-
 250 ered the empirical model proposed by Livio and Ferrario (2020) which relates the distribu-
 251 tion of triggered avalanches N_{ava} with the epicentral distance Δ :

$$G(\mathbf{m}) = N_{ava} = a \exp \left[- \left(\frac{\Delta - b}{c} \right)^2 \right], \quad (2)$$

252 where a is the amplitude of the distribution, b the distance of the peak amplitude and c the
 253 width of the distribution. While we do not have images just before and just after the event,
 254 we derived an estimation of the number of triggered avalanches from this relationship:

$$N_{ava} = \Delta n - \bar{q} \times n \Delta t / 100, \quad (3)$$

255 where \bar{q} is the long-term avalanche rate (i.e., we conservatively considered $6\% \cdot \text{MYear}^{-1}$).
 256 Because the avalanche susceptibility is not evenly distributed (i.e., steep slopes only located
 257 inside impact craters, non-homogeneous surface/sub-surface properties), we only consider
 258 observations that meet the following criteria: $\Gamma^* < 1.93$, and $\Delta t < 1.5 \text{ MYear}$, to only ac-
 259 count for the lowest thermal inertia (see Fig. 3) and the smallest time span between images
 260 to reduce biases. Then, we used a Monte Carlo method to invert the most probable epicen-
 261 ter location using a maximum likelihood function with a Laplacian distribution of errors
 262 (Mosegaard & Tarantola, 1995) (See Supp. Info. Text S4). The resulting probability dis-
 263 tribution of the epicenter under all of these considerations is given in Figure 5. It is situated
 264 in between the locations obtained from both body and surface waves analysis respectively
 265 (Kawamura et al., 2023; Panning et al., 2023; Kim et al., 2022), then included in the uncer-
 266 tainty ellipses of epicentral locations (green contours in Fig. 5).

267 This distribution can lead us to two different interpretations regarding the source mech-
 268 anism of the quake, mainly related to internal tectonic activity. A first hypothesis would
 269 be based on the fact that our distribution is slightly shifted toward the East from the wrin-
 270 kle ridges, on the flanks of Apollinaris Patera. It is now well supported that Mars still hosts
 271 remnant volcano-tectonic activity, especially along Cerberus Fossae (Giardini et al., 2020;
 272 Horvath et al., 2021; Perrin et al., 2022; Stähler et al., 2022), possibly due to the presence
 273 of a plume (Broquet & Andrews-Hanna, 2022), and associated with normal slip motion
 274 (Brinkman et al., 2021; Jacob et al., 2022). While the moment tensor analysis of the S1222a
 275 event can give very different slip motions, NNW-SSE normal faulting is a possible solution
 276 (Maguire et al., 2023), highlighting a possible activity of Apollinaris Patera at depth. How-
 277 ever, unlike Cerberus Fossae, Apollinaris Patera is an old Noachian volcano, thus it seems
 278 unlikely that remnant volcanic activity would be present at shallow depth. A second hypothe-
 279 sis would be related to the 450 km long wrinkle ridge, trending NNE-SSW, and cross-cutting
 280 the Hesperian terrains between the two epicentral locations (black lines in figure 5). The
 281 probability distribution of the epicenter inferred from the avalanche rate is about 30 to 60 km
 282 East of this major structure. The shape of the topographic profile across the ridge is an asym-
 283 metric arch-ridge, with a steep slope facing West and a shallow slope facing East (Fig. 1),
 284 which would imply a main East-dipping thrust at depth (Andrews-Hanna, 2020). Assuming
 285 a fault dip of 34° to 42° for arch-ridges (Andrews-Hanna, 2020), a probability distribution
 286 situated about 30 to 60 km East of the wrinkle ridge would lead to a hypocentral depth rang-
 287 ing from 20 to 54 km. This range of depth is in agreement with the best solutions found by
 288 Maguire et al. (2023). Along with another study by (Brinkman et al., 2023), their preferred
 289 solutions present mainly reverse slip motions striking E-W to NW-SE, which is not optimally
 290 oriented with the overall wrinkle ridge observed from orbital imagery. However, local large
 291 variations in fault strikes are possible along a wrinkle ridge. Note that the wrinkle ridges are
 292 cross-cutting a large E-W bulge situated at about -5° latitude, connecting the flanks of Apol-
 293 linaris Patera and a large crater in the west (Fig. 1). This bulge presents hundreds of meters

294 of difference in elevation and slight apparent thermal inertia anomalies that could indicate
 295 a bedrock affected by an old tectonic structure. Interestingly, the bulge's azimuth is aligned
 296 with our probability distribution of the epicenter. More work would be needed to understand
 297 the origin of this structure and a possible link with the source of the marsquake.

298 It should also be noted that source locations obtained from other methods such as sur-
 299 face waves or coda characteristics give different locations (Kim et al., 2022; Panning et al.,
 300 2023; Menina et al., 2023). Both studies using surface waves predict source locations more
 301 towards the south as shown in 5. This is due to different back azimuth they obtained for sur-
 302 face waves compared from that described in (Kawamura et al., 2023) using body waves.
 303 Panning et al. (2023) also discusses the possibility that the source location could be in the
 304 southern hemisphere. Interestingly, Menina et al. (2023) conclude that they need a thick
 305 (60km) diffusive layer to explain the coda shape of S1222a. This could imply that either
 306 the source location could be in the highlands of the southern hemisphere (Wieczorek et al.,
 307 2022), or that thermal anomalies at depth are present in the Appollinaris area.

308 Our work leads us to propose that the source of the quake is likely due to thermal con-
 309 traction due to Mars' cooling through time. The peak of thermal contraction and wrinkle
 310 ridge formation occurred during the early Hesperian and decreased progressively until now
 311 (Watters, 1993). Even if the wrinkle ridge in figure 5 is well expressed in morphology, its
 312 surface trace ends to the north, near the transition between Hesperian and Amazonian ter-
 313 rains (Tanaka et al., 2014). This indicates that the ridge has not been active in recent times.
 314 However, thermal contraction is still ongoing on Mars and might re-activate local mechanical
 315 weaknesses in the martian crust, such as wrinkle ridges, over larger recurrence time periods.
 316 If such activity is real, microseismicity should be associated with it.

317 **4 Conclusions**

318 In our comprehensive study of surface features surrounding the S1000a and S1222a
 319 seismic events on Mars, we utilized MRO orbital data to assess the associated avalanche
 320 rates. Our findings reveal a substantial increase in avalanches following the S1000a impact
 321 event, suggesting its indirect aftermaths, likely via secondary impacts. The S1222a event
 322 presented a more complex scenario, necessitating thorough investigation. We established
 323 pre-event avalanche rates in line with global estimates from Aharonson et al. (2003) and
 324 those near Olympus Mons obtained by Heyer et al. (2019), ranging between 1 and 6%.MYears⁻¹.
 325 These rates, when compared to post-event rates of up to 40%.MYear⁻¹ near the estimated
 326 epicenter (Kawamura et al., 2023; Panning et al., 2023; Kim et al., 2022), underscore a sig-
 327 nificant increase in areas of lower apparent thermal inertia. This leads us to propose that the
 328 S1222a marsquake could be the driving factor behind the observed increase in avalanches.
 329 This analysis also enabled us to estimate a probable epicenter for the marsquake, considering
 330 the Γ^* threshold of 1.5 and a radial ground acceleration. This inferred location is intriguingly
 331 situated near a volcanic edifice and a North-South wrinkle ridge, highlighting the geologi-
 332 cal complexity of the region. Our study not only might suggest that current seismic activity
 333 on Mars can initiate mass wasting processes like dust avalanches but also opens avenues for
 334 exploring regions with observed avalanches and other seismic events detected by the InSight
 335 mission. The increased rates of avalanches in areas with historical seismic sources suggest
 336 that ground deformation plays a pivotal role in these phenomena. This methodology can
 337 be invaluable in future seismic event analyses, where visible aftermaths such as avalanches
 338 can offer significant insights into epicenter locations. Overall, our findings demonstrate that
 339 avalanches on Mars serve as a crucial tool for documenting rapid processes, from discrete
 340 surface perturbations like impacts to more continuous events like quakes. This understanding
 341 significantly enhances our ability to study and interpret the dynamic surface and subsurface
 342 processes of Mars.

343 5 Acknowledgments

344 Authors thank Menina S., Margerin L., Kim D., Malystskyy D., Stähler S., Wieczorek
 345 M., Panning M. for InSightful discussions on the S1222a event. Authors thank Dundas C.M.
 346 for his help in accessing the post-event HiRISE images for both events. The authors express
 347 their gratitude to Ferrari C. for providing valuable insights into thermal inertia, to A. Spiga
 348 for his expertise on the output of General Circulation Models (GCMs), and to P. Souloumiac
 349 for her expert knowledge on slope failure conditions. Authors thank anonymous review-
 350 ers and the associate editor for their constructive feedback that substantially improved the
 351 manuscript. All authors declare no conflict of interest. French co-authors acknowledge the
 352 French Space Agency CNES and ANR (ANR-19-CE31-0008). AL, TK, PL, SR, GS, AM
 353 acknowledge Idex Paris Cité (ANR-18-IDEX-0001). IJD was funded by NASA InSight PSP
 354 grant 80NSSC20K0971.

355 6 Open Research

356 The orbital data are available online: HRSC are available at ESA's Planetary Science
 357 Archive (<https://www.cosmos.esa.int/web/psa/mars-express>). THEMIS
 358 data are available at Arizona State University's repository (<https://themis.asu.edu>).
 359 MOC images are available at the PDS Imaging Node ([https://pds-imaging.jpl
 360 .nasa.gov/data/mgs-m-moc-na_wa-2-sdp-10-v1.0/](https://pds-imaging.jpl.nasa.gov/data/mgs-m-moc-na_wa-2-sdp-10-v1.0/)). MOLA data are avail-
 361 able at the PDS Geosciences Node ([https://pds-geosciences.wustl.edu/missions/
 362 mgs/mola.html](https://pds-geosciences.wustl.edu/missions/mgs/mola.html)). Apparent thermal inertia map is provided by the USGS ([https://
 363 astrogeology.usgs.gov/maps/mars-themis-derived-global-thermal
 364 -inertia-mosaic](https://astrogeology.usgs.gov/maps/mars-themis-derived-global-thermal-inertia-mosaic)). HiRISE data, including the post-event images, are available at the
 365 University of Arizona's dedicated website (<https://www.uahirise.org>). CTX image
 366 are available at the Imaging PDS Node ([https://pds-imaging.jpl.nasa.gov/
 367 data/mro/mars_reconnaissance_orbiter/ctx/](https://pds-imaging.jpl.nasa.gov/data/mro/mars_reconnaissance_orbiter/ctx/)). The post-event CTX images
 368 will be posted on the NASA PDS by MSSS by the time of publication. Meanwhile, referee's
 369 can have access to the mosaic at [https://www.dropbox.com/sh/ulcykaotwxvi7ga/
 370 AAAsDcqw4FrkGDqjb4HTFmjka?dl=0](https://www.dropbox.com/sh/ulcykaotwxvi7ga/AAAsDcqw4FrkGDqjb4HTFmjka?dl=0). The avalanche catalogue is available on Zen-
 371 odo (doi:10.5281/zenodo.7679315). The InSight seismic event catalogue version 9 (InSight
 372 Marsquake Service, 2022) and waveform data (InSight Mars SEIS Data Service, 2019a,b)
 373 are available from the IGP Datacenter and IRIS-DMC, as are previous catalogue versions.
 374 Seismic waveforms are also available from NASA PDS. The crustal thickness grid is avail-
 375 able on Zenodo (doi:10.5281/zenodo.6477509).

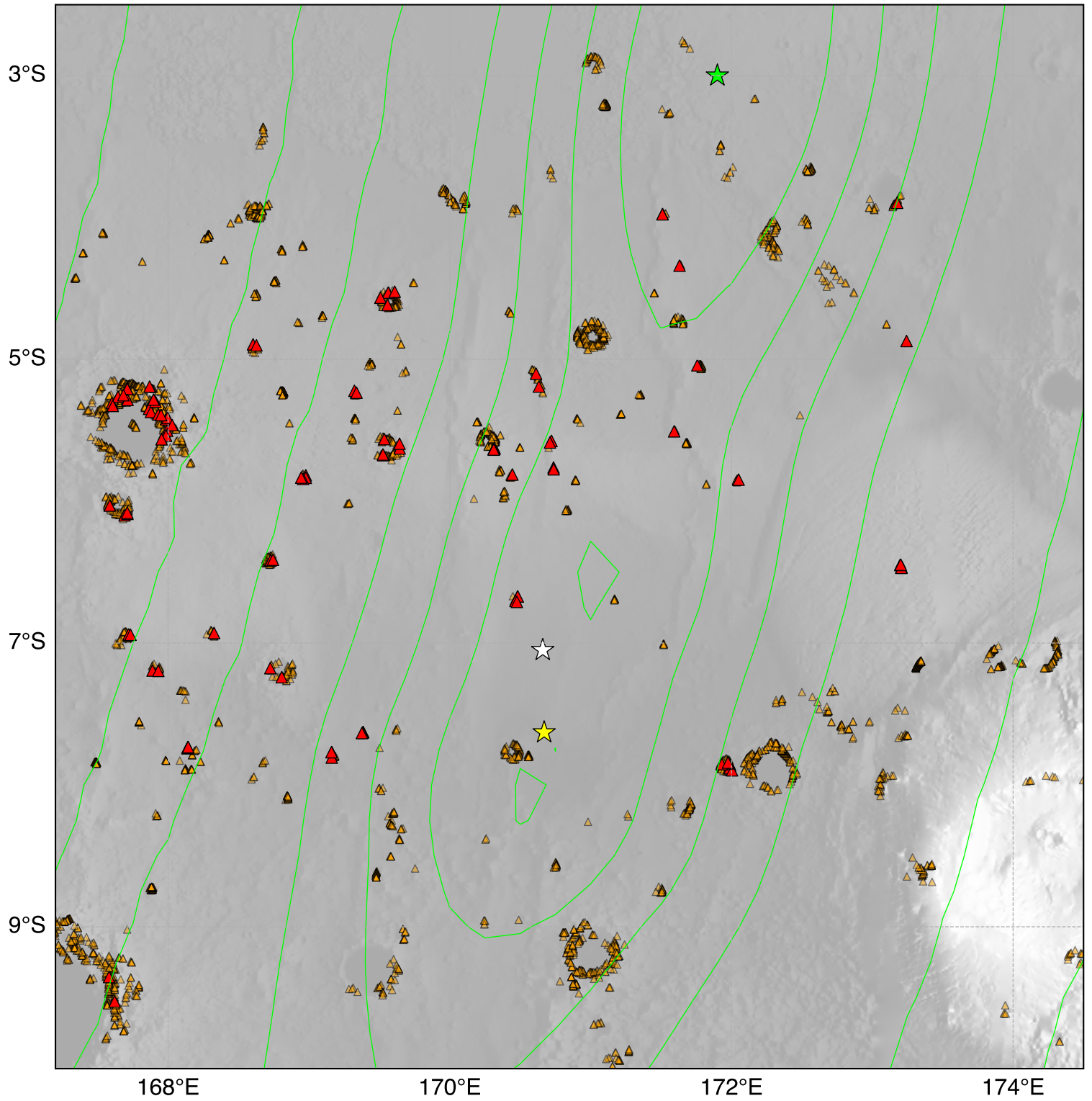


Figure 1. Regional map of dust avalanches near the S1222a event estimated location (green star with associated green contours, (Kawamura et al., 2023)). The white star is the location estimated by multi-orbit surface waves (Panning et al., 2023). The yellow star shows the estimated location according to surface waves (Kim et al., 2022). Orange symbols are all avalanches mapped. Red symbols show where avalanches are observed on post-event images. Basemap is the MOLA elevation map (Smith et al., 2001).

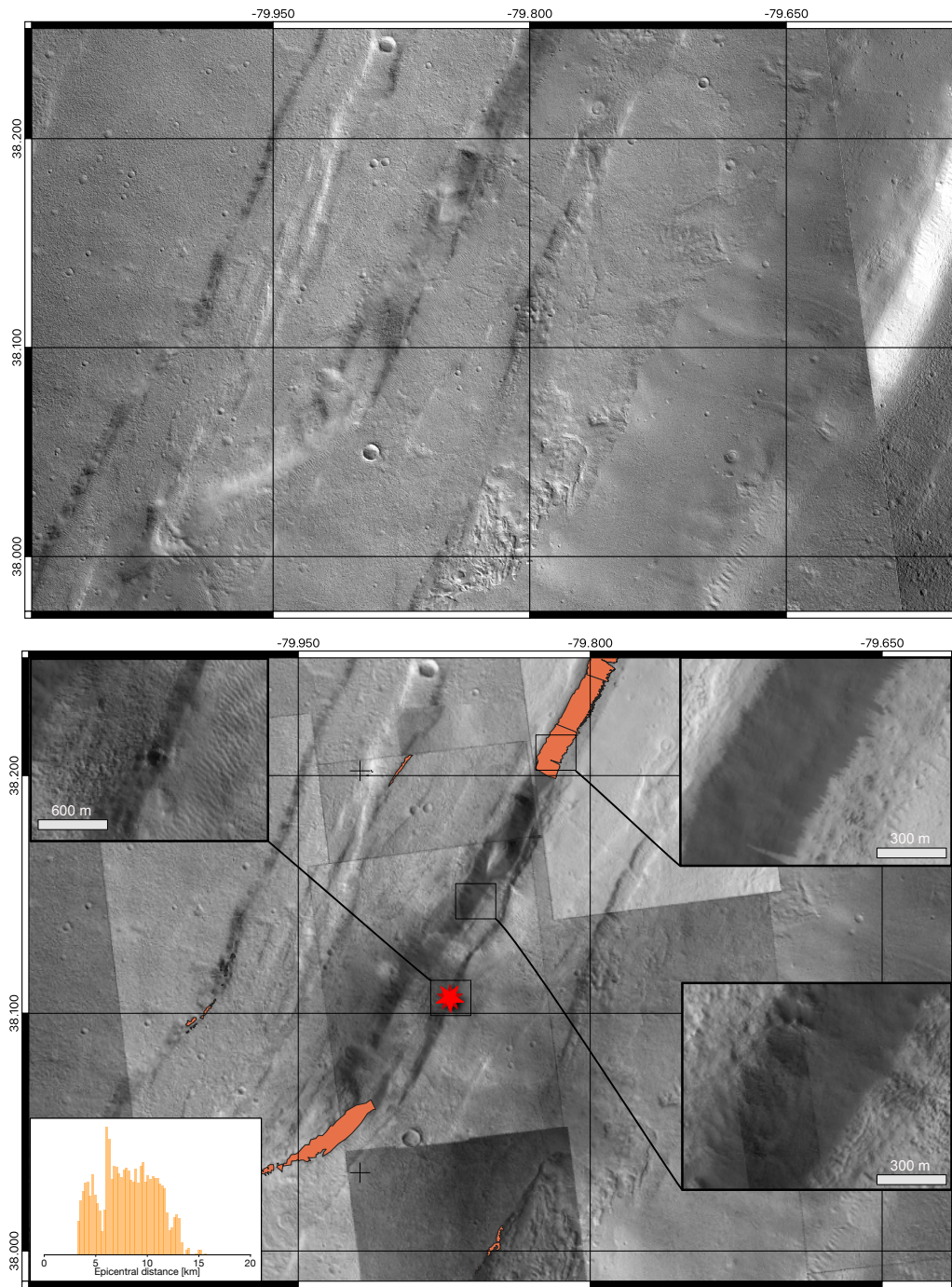


Figure 2. (top) Pre-event CTX mosaic around the impact location of S1000a (dated from 2018-09-12) showing absence of any dust avalanches. (bottom) Post-event HiRISE mosaic on top of CTX images around the impact location of S1000a event (red star) with associated triggered avalanches (orange areas). Insets show close-up on the crater, the avalanches areas and slopes without new avalanches (from top-left, to bottom-right, respectively). The density distribution of avalanches with respect to the epicentral distance is shown in the bottom-left inset.

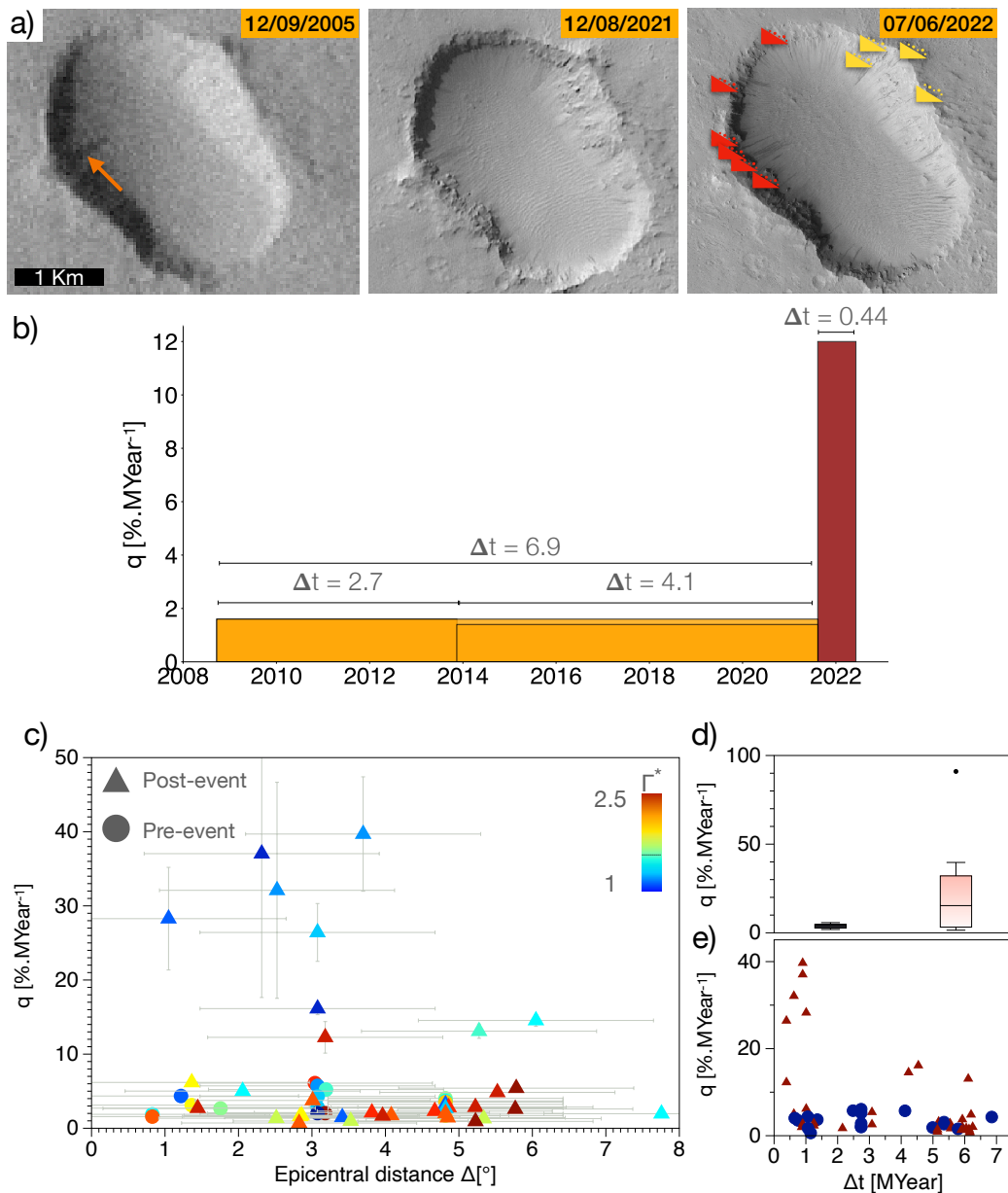


Figure 3. a) Image times series with THEMIS-Vis image V1768100 (17m/pixel) taken in 2005, CTX image N21_070520_1744_XI_05S189W (6m/pixel) taken 8 months before S1222a, and an HiRISE image (down-sampled to 5m/pixel) ESP_074357_1745 taken a few weeks after the marsquake. New avalanches marked with the red symbols. Additional doubtful avalanches are indicated with the yellow symbols, b) time series of avalanche rate q over the 2008-2022 period (orange for pre-event period, red for image pair including post-event observations). c) Avalanche rate q as a function of the epicentral distance Δ (with respect to the green star of Fig. 1) for CTX/CTX image pairs. Symbols are associated to pre-event (circles) or post-event (triangles). Color scales with the ratio of apparent thermal inertia (Γ^* , with dashed line at 1.5). d) Box plot of avalanche rates for pre-event pairs (black) and pre/post-event pairs (red). e) Avalanche rate q as a function of timespan Δt . Note that some symbols can overlap each other on both plots.

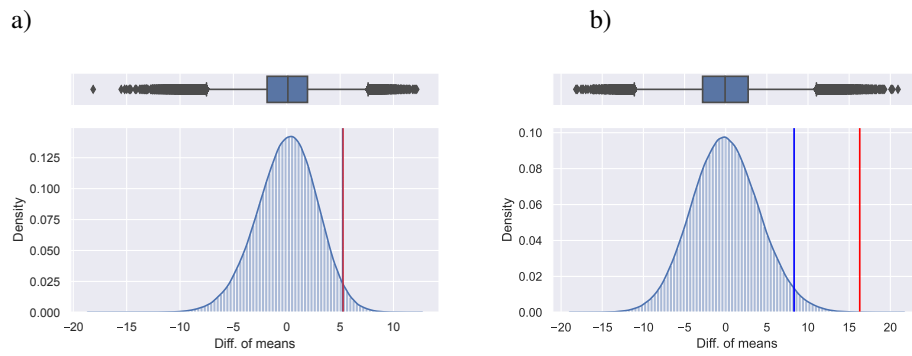


Figure 4. Bootstrapping statistics. (a) accounting for the whole data set, (b) when only considering $q > 5$ for the post-event observation. (top-panel) Quantiles of the permutation tests. (bottom-panel) The distribution of the permutation tests. The thin vertical blue lines gives the 95% of the test statistics distribution. The dashed red vertical line shows the observed statistics.

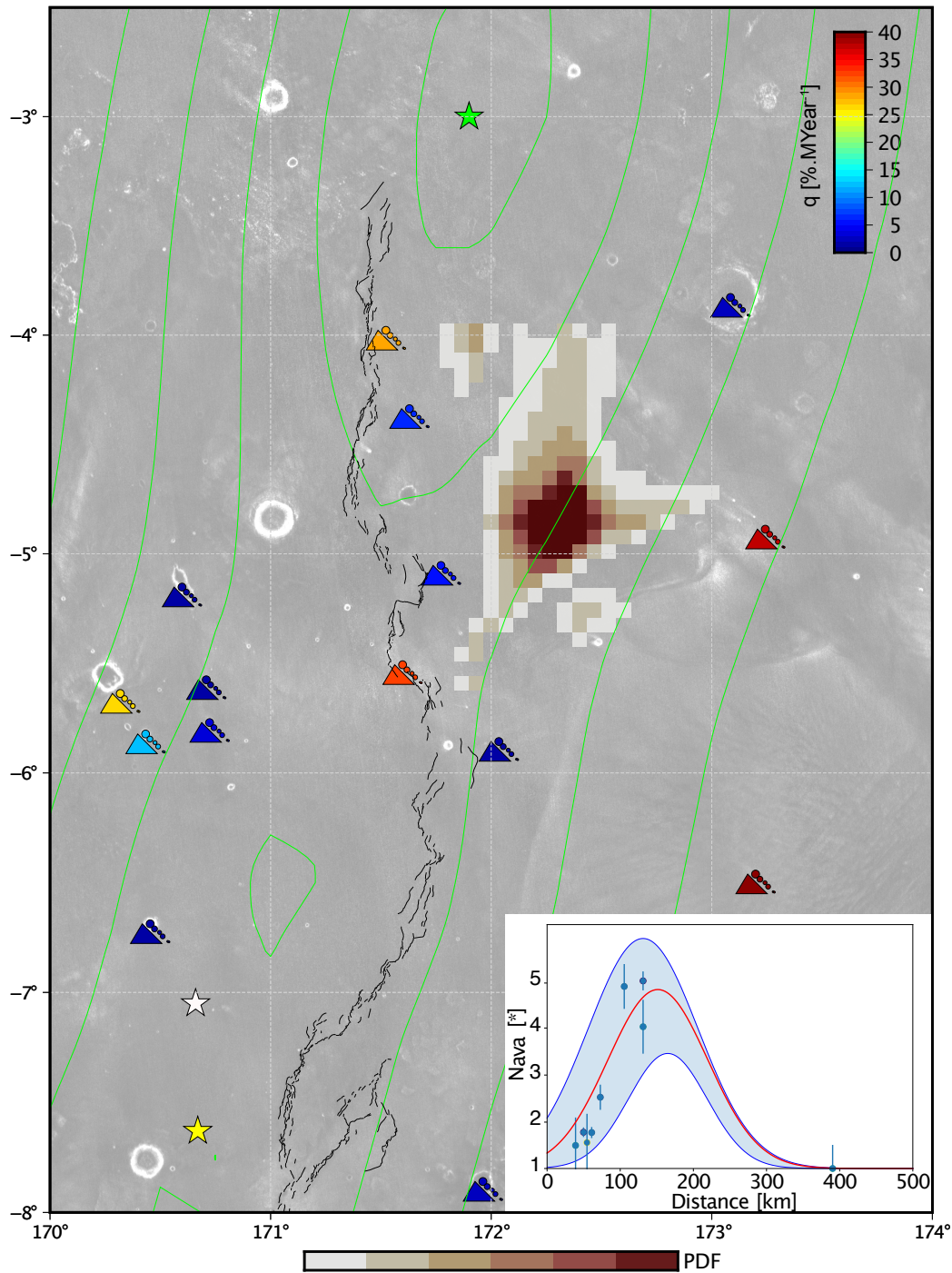


Figure 5. Probability distribution of the epicenter inferred from avalanche observations (reddish colormap). Symbols show number of avalanches observed on post-event images. Color scales with the rate q . The green star (upper center) is the maximum peak of the estimated epicenter and its uncertainty ellipses (green contours) obtained from body waves (Kawamura et al., 2023), the white star, the location estimated from multi-orbit surface waves (Panning et al., 2023), and the yellow star is the estimated epicenter derived from the surface waves (Kim et al., 2022). Black lines are detailed surface traces of the main wrinkle ridge in the vicinity of the epicentral area. Background map is the thermal inertia Γ . (Inset) Expected avalanche density distribution with confidence interval from Monte Carlo inversion using equation 2 with respect to the number of avalanche N_{ava} derived from equation 3.

376

References

377

Aharonson, O., Schorghofer, N., & Gerstell, M. F. (2003). Slope streak formation and dust deposition rates on Mars: Martian slope streak formation rates. *Journal of Geophysical Research: Planets*, 108(E12). Retrieved 2022-07-14, from <http://doi.wiley.com/10.1029/2003JE002123> doi: 10.1029/2003JE002123

378

379

380

Andrews-Hanna, J. C. (2020). The tectonic architecture of wrinkle ridges on Mars. *Icarus*, 351(October 2019), 113937. Retrieved from <https://doi.org/10.1016/j.icarus.2020.113937> doi: 10.1016/j.icarus.2020.113937

381

382

383

Banerdt, W. B., Smrekar, S. E., Banfield, D., Giardini, D., Golombek, M., Johnson, C. L., . . . Wieczorek, M. (2020, Mar 01). Initial results from the insight mission on mars. *Nature Geoscience*, 13(3), 183-189.

384

385

386

Baratoux, D., Mangold, N., Forget, F., Cord, A., Pinet, P., Daydou, Y., . . . HRSC CO- Investigator Team (2006). The role of the wind-transported dust in slope streaks activity: Evidence from the HRSC data. *Icarus*, 183(1), 30-45. doi: 10.1016/j.icarus.2006.01.023

387

388

389

Battalio, M., & Wang, H. (2021). The Mars Dust Activity Database (MDAD): A comprehensive statistical study of dust storm sequences. *Icarus*, 354, 114059. Retrieved 2022-07-14, from <https://linkinghub.elsevier.com/retrieve/pii/S001910352030405X> doi: 10.1016/j.icarus.2020.114059

390

391

392

Bergonio, J. R., Rottas, K. M., & Schorghofer, N. (2013). Properties of martian slope streak populations. *Icarus*, 225(1), 194-199. Retrieved from <https://www.sciencedirect.com/science/article/pii/S0019103513001395> doi: <https://doi.org/10.1016/j.icarus.2013.03.023>

393

394

395

Bhardwaj, A., Sam, L., Martín-Torres, F. J., Zorzano, M.-P., & Fonseca, R. M. (2017). Martian slope streaks as plausible indicators of transient water activity. *Scientific Reports*, 7(1), 7074. Retrieved from <https://doi.org/10.1038/s41598-017-07453-9> doi: 10.1038/s41598-017-07453-9

396

397

398

Bhardwaj, A., Sam, L., Martín-Torres, F. J., & Zorzano, M.-P. (2019). Are slope streaks indicative of global-scale aqueous processes on contemporary mars? *Reviews of Geophysics*, 57(1), 48-77. doi: <https://doi.org/10.1029/2018RG000617>

399

400

401

Bontemps, N., Lacroix, P., Larose, E., Jara, J., & Taïpe, E. (2020). Rain and small earthquakes maintain a slow-moving landslide in a persistent critical state. *Nature Communications*, 11(1), 780.

402

403

404

Brinkman, N., Sollberger, D., Schmelzbach, C., Stähler, S. C., & Robertsson, J. (2023). Applications of time-frequency domain polarization filtering to insight seismic data. *Earth and Space Science*, 10(11), e2023EA003169.

405

406

407

Brinkman, N., Stähler, S. C., Giardini, D., Schmelzbach, C., Khan, A., Jacob, A., . . . Banerdt, W. B. (2021). First focal mechanisms of marsquakes. *Journal of Geophysical Research: Planets*. Retrieved from <https://agupubs.onlinelibrary.wiley.com/doi/abs/10.1029/2020JE006546> doi: <https://doi.org/10.1029/2020JE006546>

408

409

410

Broquet, A., & Andrews-Hanna, J. C. (2022). Geophysical evidence for an active mantle plume underneath Elysium Planitia on Mars. *Nature Astronomy*. doi: 10.1038/s41550-022-01836-3

411

412

413

Brown, J., & Roberts, G. (2019). Possible evidence for variation in magnitude for marsquakes from fallen boulder populations, Grjota Valles, Mars. *J. Geophys. Res. Planets*, 124(3), 801-812. doi: 10.1029/2018JE005622

414

415

416

Burleigh, K. J., Melosh, H. J., Tornabene, L. L., Ivanov, B., McEwen, A. S., & Daubar, I. J. (2012). Impact airblast triggers dust avalanches on mars. *Icarus*, 217(1), 194-201.

417

418

419

Böse, M., Stähler, S. C., Deichmann, N., Giardini, D., Clinton, J., Lognonné, P., . . . Banerdt, W. B. (2021, 06). Magnitude Scales for Marsquakes Calibrated from InSight Data. *Bulletin of the Seismological Society of America*, 111(6), 3003-3015.

420

421

422

Ceylan, S., Clinton, J. F., Giardini, D., Stähler, S. C., Horleston, A., Kawamura, T., . . .

423

424

425

Banerdt, W. B. (2022). The marsquake catalogue from insight, sols 0–1011. *Physics of the Earth and Planetary Interiors*, 333, 106943.

426

427

428

429

430

- 431 Chen, X.-l., Shan, X., Wang, M.-m., Liu, C.-g., & Han, N.-n. (2020, 03). Distribution pat-
 432 tern of coseismic landslides triggered by the 2017 jiuzhaigou ms 7.0 earthquake of
 433 china: Control of seismic landslide susceptibility. *ISPRS International Journal of*
 434 *Geo-Information*, 9, 198. doi: 10.3390/ijgi9040198
- 435 Christensen, P. R., Bandfield, J. L., Hamilton, V. E., Ruff, S. W., Kieffer, H. H., Titus, T. N.,
 436 . . . Greenfield, M. (2001). Mars global surveyor thermal emission spectrometer exper-
 437 iment: Investigation description and surface science results. *Journal of Geophysical*
 438 *Research: Planets*, 106(E10), 23823-23871.
- 439 Christensen, P. R., Jakosky, B. M., Kieffer, H. H., Malin, M. C., Jr, H. Y. M., Nealon, K.,
 440 . . . Ravine, M. (2004). The thermal emission imaging system (themis) for the mars
 441 2001 odyssey mission. In C. T. Russell (Ed.), *2001 mars odyssey* (pp. 85–130). Dor-
 442 drecht: Springer Netherlands.
- 443 Chuang, F. C., Beyer, R. A., McEwen, A. S., & Thomson, B. J. (2007). HiRISE observa-
 444 tions of slope streaks on mars. *Geophysical Research Letters*, 34(20). Retrieved from
 445 [https://agupubs.onlinelibrary.wiley.com/doi/abs/10.1029/](https://agupubs.onlinelibrary.wiley.com/doi/abs/10.1029/2007GL031111)
 446 [2007GL031111](https://doi.org/10.1029/2007GL031111) doi: <https://doi.org/10.1029/2007GL031111>
- 447 Clinton, J. F., Ceylan, S., van Driel, M., Giardini, D., Stähler, S. C., Böse, M., . . . Stott, A. E.
 448 (2021). The marsquake catalogue from insight, sols 0–478. *Physics of the Earth and*
 449 *Planetary Interiors*, 310, 106595.
- 450 Davison, A. C., & Hinkley, D. V. (1997). *Bootstrap methods and their application*. Cam-
 451 bridge University Press.
- 452 Dundas, C. M. (2020). Geomorphological evidence for a dry dust avalanche origin of slope
 453 streaks on mars. *Nature Geoscience*, 13(7), 473–476. Retrieved from [https://](https://doi.org/10.1038/s41561-020-0598-x)
 454 doi.org/10.1038/s41561-020-0598-x doi: 10.1038/s41561-020-0598-x
- 455 Durand, V., Mangeney, A., Bernard, P., Bonilla, L. F., Satriano, C., Jia, X., . . . Hibert, C.
 456 (Minor revision). The competing role of seismicity and rainfall in slope destabiliza-
 457 tion: rockfalls triggered on a metastable volcanic edifice. *Science Advances*.
- 458 Efron, B., & Tibshirani, R. J. (1993). *An introduction to the bootstrap*. CRC Press.
- 459 Ferguson, R. L., Christensen, P. R., & Kieffer, H. H. (2006, dec). High-resolution ther-
 460 mal inertia derived from the Thermal Emission Imaging System (THEMIS): Thermal
 461 model and applications. *Journal of Geophysical Research: Planets*, 111(E12), n/a–n/a.
 462 Retrieved from <http://doi.wiley.com/10.1029/2006JE002735> doi:
 463 [10.1029/2006JE002735](https://doi.org/10.1029/2006JE002735)
- 464 Ferguson, H. M., & Lucchitta, B. K. (1984). *Dark streaks on talus slopes, Mars*. In NASA.
 465 Washington Rept. of Planetary Geol. Programs p 188-190 (SEE N84-23431 13-91).
- 466 Fernando, B., Daubar, I. J., Charalambous, C., Grindrod, P. M., Stott, A., Al Ateqi, A., . . .
 467 Banerdt, W. B. (2023). A Tectonic Origin for the Largest Marsquake Observed by
 468 InSight. *Geophysical Research Letters*, 50(20), 1–10. doi: 10.1029/2023GL103619
- 469 Ferris, J. C., Dohm, J. M., Baker, V. R., & Maddock III, T. (2002). Dark slope streaks
 470 on mars: Are aqueous processes involved? *Geophysical Research Letters*, 29(10),
 471 128-1-128-4. Retrieved from [https://agupubs.onlinelibrary.wiley](https://agupubs.onlinelibrary.wiley.com/doi/abs/10.1029/2002GL014936)
 472 [.com/doi/abs/10.1029/2002GL014936](https://doi.org/10.1029/2002GL014936) doi: [https://doi.org/10.1029/](https://doi.org/10.1029/2002GL014936)
 473 [2002GL014936](https://doi.org/10.1029/2002GL014936)
- 474 Gerstell, M. F., Aharonson, O., & Schorghofer, N. (2004). A distinct class of avalanche
 475 scars on Mars. *Icarus*, 168(1), 122–130. Retrieved 2022-07-14, from [https://](https://linkinghub.elsevier.com/retrieve/pii/S0019103503003907)
 476 linkinghub.elsevier.com/retrieve/pii/S0019103503003907 doi:
 477 [10.1016/j.icarus.2003.11.005](https://doi.org/10.1016/j.icarus.2003.11.005)
- 478 Giardini, D., Lognonné, P., Banerdt, W., Pike, W., Christensen, U., Ceylan, S., . . . Yana., C.
 479 (2020). The Seismicity of Mars. *Nature Geoscience*, 13(3), 205–212. doi: [http://](http://doi.org/10.1038/s41561-020-0539-8)
 480 doi.org/10.1038/s41561-020-0539-8
- 481 Head, J. W., Marchant, D. R., Dickson, J. L., Levy, J. S., & Morgan, G. A. (2007, March).
 482 Slope Streaks in the Antarctic Dry Valleys: Characteristics, Candidate Formation
 483 Mechanisms, and Implications for Slope Streak Formation in the Martian Environ-
 484 ment. In *38th annual lunar and planetary science conference* (p. 1935).
- 485 Heyer, T., Kreslavsky, M., Hiesinger, H., Reiss, D., Bernhardt, H., & Jaumann, R. (2019).

- 486 Seasonal formation rates of martian slope streaks. *Icarus*, 323, 76–86. Retrieved
487 2022-07-14, from [https://linkinghub.elsevier.com/retrieve/pii/
488 S0019103518306857](https://linkinghub.elsevier.com/retrieve/pii/S0019103518306857) doi: 10.1016/j.icarus.2019.01.010
- 489 Heyer, T., Raack, J., Hiesinger, H., & Jaumann, R. (2020). Dust devil triggering of
490 slope streaks on mars. *Icarus*, 351, 113951. Retrieved from [https://www
491 .sciencedirect.com/science/article/pii/S0019103520303249](https://www.sciencedirect.com/science/article/pii/S0019103520303249)
492 doi: <https://doi.org/10.1016/j.icarus.2020.113951>
- 493 Horvath, D. G., Moitra, P., Hamilton, C. W., Craddock, R. A., & Andrews-Hanna, J. C.
494 (2021, September). Evidence for geologically recent explosive volcanism in Elysium
495 Planitia, Mars. *Icarus*, 365, 114499. doi: 10.1016/j.icarus.2021.114499
- 496 InSight Marsquake Service. (2022). *Mars seismic catalogue, insight mission; v12 2022-10-
497 01*. ETHZ, IGP, JPL, ICL, Univ. Bristol. Retrieved from [https://www.insight
498 .ethz.ch/seismicity/catalog/v12](https://www.insight.ethz.ch/seismicity/catalog/v12) doi: 10.12686/a18
- 499 Jacob, A., Plasman, M., Perrin, C., Fuji, N., Lognonné, P., Xu, Z., . . . Banerdt, W. (2022).
500 Seismic sources of insight marsquakes and seismotectonic context of elysium
501 planitia, mars. *Tectonophysics*, 837, 229434. Retrieved from [https://www
502 .sciencedirect.com/science/article/pii/S0040195122002281](https://www.sciencedirect.com/science/article/pii/S0040195122002281)
503 doi: <https://doi.org/10.1016/j.tecto.2022.229434>
- 504 Kawamura, T., Clinton, J., Zenhäusern, G., Ceylan, S., Horleston, A., Dahmen, N., . . .
505 Banerdt, W. (2023). S1222a - the largest Marsquake detected by InSight. *Geophysical
506 Research Letters*. doi: 10.1029/2022GL101543
- 507 Kim, D., Stähler, S. C., Ceylan, S., Lekic, V., Maguire, R., Zenhäusern, G., . . . Banerdt,
508 W. B. (2022). Structure along the martian dichotomy constrained by rayleigh and
509 love waves and their overtones. *Geophysical Research Letters*, e2022GL101666.
- 510 Knapmeyer, M., Oberst, J., Hauber, E., Wählisch, M., Deuchler, C., & Wagner, R. (2006).
511 Working models for spatial distribution and level of Mars' seismicity. *J. Geophys. Res.
512 E Planets*, 111(11), 1–23. doi: 10.1029/2006JE002708
- 513 Knapmeyer, M., Stähler, S., Plesa, A.-C., Ceylan, S., Charalambous, C., Clinton, J., . . .
514 Banerdt, W. B. (2023). The global seismic moment rate of mars after event s1222a.
515 *Geophysical Research Letters*, 50(7), e2022GL102296.
- 516 Kreslavsky, M. A., & Head, J. W. (2009). Slope streaks on Mars: A new "wet" mechanism.
517 *Icarus*, 201(2), 517–527. Retrieved 2022-07-14, from [https://linkinghub
518 .elsevier.com/retrieve/pii/S0019103509000608](https://linkinghub.elsevier.com/retrieve/pii/S0019103509000608) doi: 10.1016/j
519 .icarus.2009.01.026
- 520 Livio, F., & Ferrario, M. F. (2020). Assessment of attenuation regressions for earthquake-
521 triggered landslides in the italian apennines: insights from recent and historical events.
522 *Landslides*, 17(12), 2825–2836.
- 523 Lognonné, P., Banerdt, W. B., Giardini, D., Pike, W. T., Christensen, U., Laudet, P., . . .
524 Wookey, J. (2019, feb). SEIS: Insight's Seismic Experiment for Internal Structure of
525 Mars. *Space Science Reviews*, 215(1), 12. Retrieved from [http://dx.doi.org/
526 10.1007/s11214-018-0574-6](http://dx.doi.org/10.1007/s11214-018-0574-6)[http://link.springer.com/10.1007/
527 s11214-018-0574-6](http://link.springer.com/10.1007/s11214-018-0574-6) doi: 10.1007/s11214-018-0574-6
- 528 Lombardo, L., & Tanyas, H. (2022). From scenario-based seismic hazard to scenario-based
529 landslide hazard: fast-forwarding to the future via statistical simulations. *Stoch Envi-
530 ron Res Risk Assess*, 36, 2229–2242.
- 531 Lucas, A. (2010). *Dynamique des instabilités gravitaires par modélisation et télédétec-
532 tion: Applications aux exemples martiens* (Theses, Institut de physique du globe de
533 paris - IGP). Retrieved from [https://tel.archives-ouvertes.fr/
534 tel-00503212](https://tel.archives-ouvertes.fr/tel-00503212)
- 535 Lucas, A., & Mangeney, A. (2007). Mobility and topographic effects for large valles
536 marineris landslides on mars. *Geophysical Research Letters*, 34(10).
- 537 Lucas, A., Mangeney, A., & Ampuero, J. P. (2014). Frictional velocity-weakening in land-
538 slides on earth and on other planetary bodies. *Nature Communications*, 5(1), 3417.
- 539 Lucas, A., Mangeney, A., Mège, D., & Bouchut, F. (2011). Influence of the scar geometry
540 on landslide dynamics and deposits: Application to martian landslides. *Journal of*

- 541 *Geophysical Research: Planets*, 116(E10).
- 542 Maguire, R. R., Lekić, V., Schmerr, N. C., Kim, D., Li, J., Beghein, C., . . . Bruce Banerdt,
543 W. (2023). Moment Tensor Estimation of Event S1222a and Implications for Tec-
544 tonics Near the Dichotomy Boundary in Southern Elysium Planitia Mars. *Journal of*
545 *Geophysical Research E: Planets*, submitted.
- 546 Malin, M. C., Bell, J. F., Cantor, B. A., Caplinger, M. A., Calvin, W. M., Clancy, R. T., . . .
547 Wolff, M. J. (2007, may). Context Camera Investigation on board the Mars Re-
548 connaissance Orbiter. *Journal of Geophysical Research*, 112(E5), E05S04. Re-
549 trieved from <http://doi.wiley.com/10.1029/2006JE002808> doi:
550 10.1029/2006JE002808
- 551 Malin, M. C., Danielson, G. E., Ingersoll, A. P., Masursky, H., Veverka, J., Ravine, M. A., &
552 Soulanille, T. A. (1992). Mars observer camera. *Journal of Geophysical Research:*
553 *Planets*, 97(E5), 7699-7718.
- 554 Martino, S., Fiorucci, M., Marmoni, G. M., Casaburi, L., Antonielli, B., & Mazzanti, P.
555 (2022). Increase in landslide activity after a low-magnitude earthquake as inferred
556 from dInSAR interferometry. *Scientific Reports*, 12(1), 2686.
- 557 McEwen, A. S., Eliason, E. M., Bergstrom, J. W., Bridges, N. T., Hansen, C. J., Delamere,
558 W. A., . . . Weitz, C. M. (2007, may). Mars Reconnaissance Orbiter's High Resolution
559 Imaging Science Experiment (HiRISE). *Journal of Geophysical Research*, 112(E5),
560 E05S02. Retrieved from <http://doi.wiley.com/10.1029/2005JE002605>
561 doi: 10.1029/2005JE002605
- 562 Menina, S., Margerin, L., Kawamura, T., Heller, G., Drilleau, M., Xu, Z., . . . Banerdt, W. B.
563 (2023). Stratification of heterogeneity in the lithosphere of Mars from envelope mod-
564 eling of event S1222a and near impacts: Interpretation and implications for very-high-
565 frequency events. *Geophysical Research Letters*, 50(7), e2023GL103202.
- 566 Miyamoto, H. (2004). Fluid dynamical implications of anastomosing slope streaks
567 on Mars. *Journal of Geophysical Research*, 109(E6), E06008. Retrieved 2022-
568 07-14, from <http://doi.wiley.com/10.1029/2003JE002234> doi:
569 10.1029/2003JE002234
- 570 Mosegaard, K., & Tarantola, A. (1995). Monte Carlo sampling of solutions to inverse prob-
571 lems. *Journal of Geophysical Research: Solid Earth*, 100(B7), 12431-12447. doi:
572 <https://doi.org/10.1029/94JB03097>
- 573 Neukum, G., & Jaumann, R. (2004). The high resolution stereo camera of Mars Express. *ESA*
574 *Special Publication*, 1240, 1-19.
- 575 Panning, M. P., Banerdt, W. B., Beghein, C., Carrasco, S., Ceylan, S., Clinton, J. F., . . . Zen-
576 häusern, G. (2023). Locating the largest event observed on Mars with multi-orbit
577 surface waves. *Geophysical Research Letters*, 50(1), e2022GL101270.
- 578 Perrin, C., Jacob, A., Lucas, A., Myhill, R., Hauber, E., Batov, A., . . . Fuji, N. (2022). Ge-
579 ometry and segmentation of Cerberus fossae, Mars: Implications for Marsquake proper-
580 ties. *J. Geophys. Res.: Planets*, 127(1), e2021JE007118. doi: [https://doi.org/10.1029/](https://doi.org/10.1029/2021JE007118)
581 2021JE007118
- 582 Phillips, C. B., Burr, D. M., & Beyer, R. A. (2007). Mass movement within a slope streak on
583 Mars. *Geophysical Research Letters*, 34(21). Retrieved from [https://agupubs](https://agupubs.onlinelibrary.wiley.com/doi/abs/10.1029/2007GL031577)
584 [.onlinelibrary.wiley.com/doi/abs/10.1029/2007GL031577](https://agupubs.onlinelibrary.wiley.com/doi/abs/10.1029/2007GL031577) doi:
585 <https://doi.org/10.1029/2007GL031577>
- 586 Posiolova, L. V., Lognonné, P., Banerdt, W. B., Clinton, J., Collins, G. S., Kawamura, T., . . .
587 Zenhäusern, G. (2022). Largest recent impact craters on Mars: Orbital imaging and
588 surface seismic co-investigation. *Science*, 378(6618), 412-417.
- 589 Roberts, G. P., Matthews, B., Bristow, C., Guerrieri, L., & Vetterlein, J. (2012, February).
590 Possible evidence of paleomarsquakes from fallen boulder populations, Cerberus Fos-
591 sae, Mars. *J. Geophys. Res. Planets*, 117(E2), n/a-n/a. doi: 10.1029/2011JE003816
- 592 Rosser, N., Kincey, M., Oven, K., Densmore, A., Robinson, T., Pujara, D. S., . . . Dhital,
593 M. R. (2021). Changing significance of landslide hazard and risk after the 2015 Mw
594 7.8 Gorkha, Nepal earthquake. *Progress in Disaster Science*, 10, 100159.
- 595 Schorghofer, N., Aharonson, O., Gerstell, M., & Tatsumi, L. (2007). Three decades of slope

- 596 streak activity on mars. *Icarus*, 191(1), 132-140. Retrieved from <https://www>
 597 [.sciencedirect.com/science/article/pii/S0019103507001960](https://www.sciencedirect.com/science/article/pii/S0019103507001960)
 598 doi: <https://doi.org/10.1016/j.icarus.2007.04.026>
- 599 Schorghofer, N., Aharonson, O., & Khatiwala, S. (2002). Slope streaks on Mars: Cor-
 600 relations with surface properties and the potential role of water: Slope streaks on
 601 Mars. *Geophysical Research Letters*, 29(23), 41–1–41–4. Retrieved 2022-07-14,
 602 from <http://doi.wiley.com/10.1029/2002GL015889> doi: 10.1029/
 603 2002GL015889
- 604 Schorghofer, N., & King, C. M. (2011). Sporadic formation of slope streaks on Mars.
 605 *Icarus*, 216(1), 159–168. Retrieved 2022-07-14, from <https://linkinghub>
 606 [.elsevier.com/retrieve/pii/S0019103511003459](https://linkinghub.elsevier.com/retrieve/pii/S0019103511003459) doi: 10.1016/
 607 j.icarus.2011.08.028
- 608 Smith, D. E., Zuber, M. T., Frey, H. V., Garvin, J. B., Head, J. W., Muhleman, D. O., ...
 609 Sun, X. (2001). Mars orbiter laser altimeter: Experiment summary after the first
 610 year of global mapping of mars. *Journal of Geophysical Research: Planets*, 106(E10),
 611 23689-23722.
- 612 Stähler, S. C., Mittelholz, A., Perrin, C., Kawamura, T., Kim, D., Knapmeyer, M., ...
 613 Banerdt, W. B. (2022). Tectonics of Cerberus Fossae unveiled by marsquakes. *Na-*
 614 *ture Astronomy*, 6(12), 1376–1386. doi: 10.1038/s41550-022-01803-y
- 615 Sullivan, R., Thomas, P., Veverka, J., Malin, M., & Edgett, K. S. (2001). Mass movement
 616 slope streaks imaged by the mars orbiter camera. *Journal of Geophysical Research:*
 617 *Planets*, 106(E10), 23607-23633. doi: <https://doi.org/10.1029/2000JE001296>
- 618 Tanaka, K., Skinner, J., Jr., D., J.M., I., Irwin R.P., Kolb, E., Fortezzo, C., ... Hare, T.
 619 (2014). Geologic map of mars. *U.S. Geological Survey Scientific, pamphlet 43 p.*
 620 doi: 10.3133/sim3292
- 621 Tatar, L. (2010). *Statistical analysis of triggered landslides : implications for earthquake*
 622 *and weather controls* (Unpublished doctoral dissertation). University of Canterbury
 623 and Université de Grenoble.
- 624 Valantinas, A., Becerra, P., Pommerol, A., Tornabene, L., Affolter, L., Cremonese, G.,
 625 ... Thomas, N. (2021). CaSSIS color and multi-angular observations of Mar-
 626 tian slope streaks. *Planetary and Space Science*, 209, 105373. Retrieved 2022-
 627 07-14, from [https://linkinghub.elsevier.com/retrieve/pii/](https://linkinghub.elsevier.com/retrieve/pii/S0032063321002129)
 628 [S0032063321002129](https://linkinghub.elsevier.com/retrieve/pii/S0032063321002129) doi: 10.1016/j.pss.2021.105373
- 629 Watters, T. R. (1993). Compressional tectonism on Mars. *Journal of Geophysical Re-*
 630 *search*, 98(E9), 17049. Retrieved from [http://doi.wiley.com/10.1029/](http://doi.wiley.com/10.1029/93JE01138)
 631 [93JE01138](http://doi.wiley.com/10.1029/93JE01138) doi: 10.1029/93JE01138
- 632 Wicczorek, M. A., Broquet, A., McLennan, S. M., Rivoldini, A., Golombek, M., Antonan-
 633 geli, D., ... Banerdt, W. B. (2022). Insight constraints on the global character of the
 634 martian crust. *Journal of Geophysical Research: Planets*, 127(5), e2022JE007298.

Supporting Information for "Discussion of possible seismically triggered avalanches after the S1222a Marsquake and S1000a impact event"

Lucas A.¹, Daubar I. J.², Le Teuff M.¹, Perrin C.³, Kawamura T.¹, Posiolova L.⁴, Lognonné P.¹,
Rodriguez S.¹, Giardini D.⁵, Sainton G.¹, Mangeney A.¹, McEwen A.⁶

Contents of this file

1. Text S1 to S4
2. Figures S1 to S8

Text S1. Note on post-marsquake image request and mapping

Once the S1222a event were recorded and a estimate of the location was provided, we investigate the orbital image archive for checking if either this location were falling into a region showing specific surface features (tectonics or avalanche signatures). It appears that this fairly flat region showing a few impact craters, into which, dust avalanches were detectable (Fig. S1). We therefore initiate the mapping using CTX and HiRISE images in order to established the list of location of interest. Then we request to MRO's team to target those specific places. As we focus on maximising the temporal coverage, we utilized all released images from MOC, THEMIS-Vis, CTX and HiRISE sensors. This leads to various conditions of observation (i.e., emission angle, local time etc.) and hence large parallax effects, especially on steep slopes areas where avalanches occur (i.e., typically from 30 to 8 degrees).

Consequently, the accuracy of the ortho-rectification performed with ISIS using either MOLA (Smith et al.; 2001), and/or HRSC DTMs (Neukum and Jaumann; 2004), is not sufficient for accurate sub-pixel co-registration between all the images, even with bundle adjustment. This is an important aspect because as a result no automatic method could be used successfully (i.e., all of our principal component analysis (PCA) and Convolutional Neural Network (CNN) attempts failed to reach the required accuracy that could be achieved with human inspection).

We manually map all avalanches in the region shown in Fig. 1 in a Geographical Information System (GIS). Then each pair of overlapping images (mostly CTX/CTX pairs, but we also considered CTX/HiRISE and HiRISE/HiRISE overlapping observations) leads to a detection of new (or absence of new) avalanches. This mapping work has been conducted by two independent people to compare and validate the results. Although non-MRO images offer a greater historical depth (~15 Earth years), the resolutions are very different between these sensors. Hence, over the 2008-2022 period, only CTX and HiRISE are considered. We down-sample the HiRISE data to 6 m/pixel, a pixel scale close to CTX's.

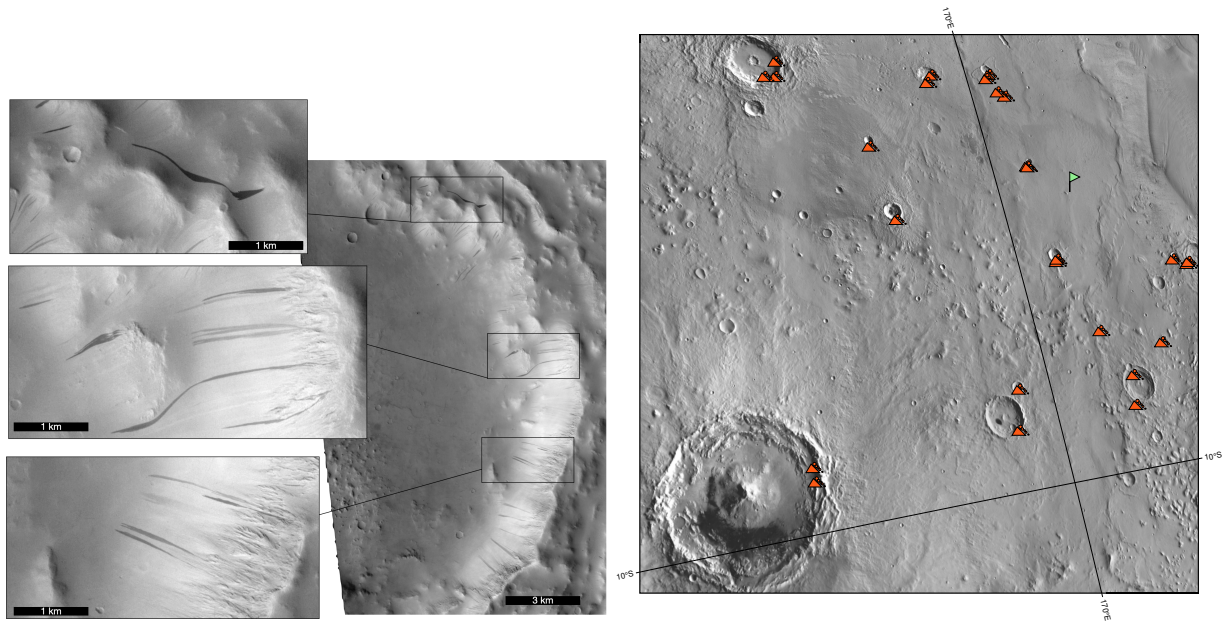


Figure S1: Location of the pre-event avalanche mapping once an estimate of the S1222a location was provided. (left panel) close up on CTX G10_021978_1748_XI_05S192W (2011-04-05).

As well known, the brightness of these streaks is usually inversely proportional to their age. The darker they are, the more recently they formed (Sullivan et al.; 2001). Note that we observe a very slow fading rate in this area, as some image pairs spanning 18 Earth years still show the same avalanches. Such a low fading rate allows us to estimate the long-term avalanche formation rate without concern that ongoing fading would significantly affect our measured rates (Aharonson et al.; 2003). Additionally, this slow fading rate is in good agreement with the dust activity reported in this region (Battalio and Wang; 2021).

For the sake of comparison, the fading rate of dust devil tracks at the InSight landing site was also measured. There, dust devil tracks fade in a few months to almost two terrestrial years (Perrin et al.; 2020). Notwithstanding, these are not formed by the same processes and thus might not fade at the same rates, in particular since avalanches remove a thicker layer of dust cover compared to dust devils. Other types of albedo features fade at different rates on Mars. For example, blast zones around new impacts have a median fading lifetime of 8 Mars years (Daubar et al.; 2016), while dust devil tracks and rover tracks fade much more quickly as they remove dust more superficially (Balme et al.; 2003; Verba et al.; 2010; Geissler et al.; 2010). To compare the same type of feature as studied here, other slope streaks have shown gradual fading over approximately 20 Mars years (e.g., Schorghofer et al.; 2007; Bergonio et al.; 2013).

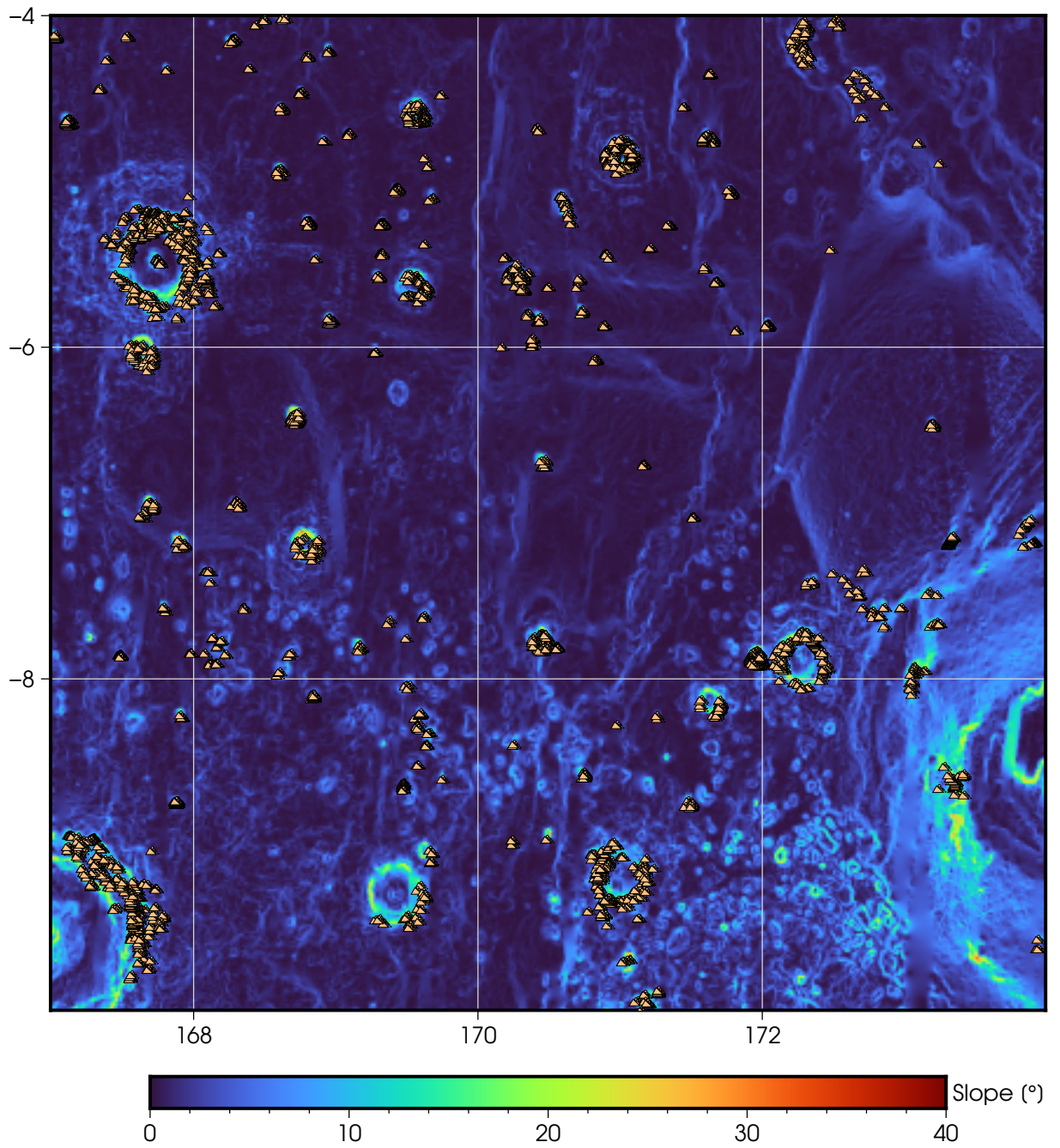


Figure S2: Slope map derived from MOLA 128ppd (Smith et al.; 2001). Orange symbols show location of avalanches over the 2005-2021 period.

Text S2. Note on the thermal inertia

The thermal inertia (Γ) is a complex data set that is not directly obtained from observations (see <https://astrogeology.usgs.gov/maps/mars-themis-derived-global-thermal-inertia-mosaic>). Numerous factors contribute to thermal inertia. In our study, however, the emphasis is on the consistency of observations. We have conducted thorough verifications to ensure homogeneity in the slopes within the areas where avalanches were mapped. This implies that any topographic effects would uniformly impact these areas. By using flat terrain as a reference for comparison, the validity of our comparative analysis of the $\Gamma^* = \Gamma_{avalanche}/\Gamma_{plain}$ across the avalanche-affected areas is maintained. The map of the Γ is given in Figure S3.

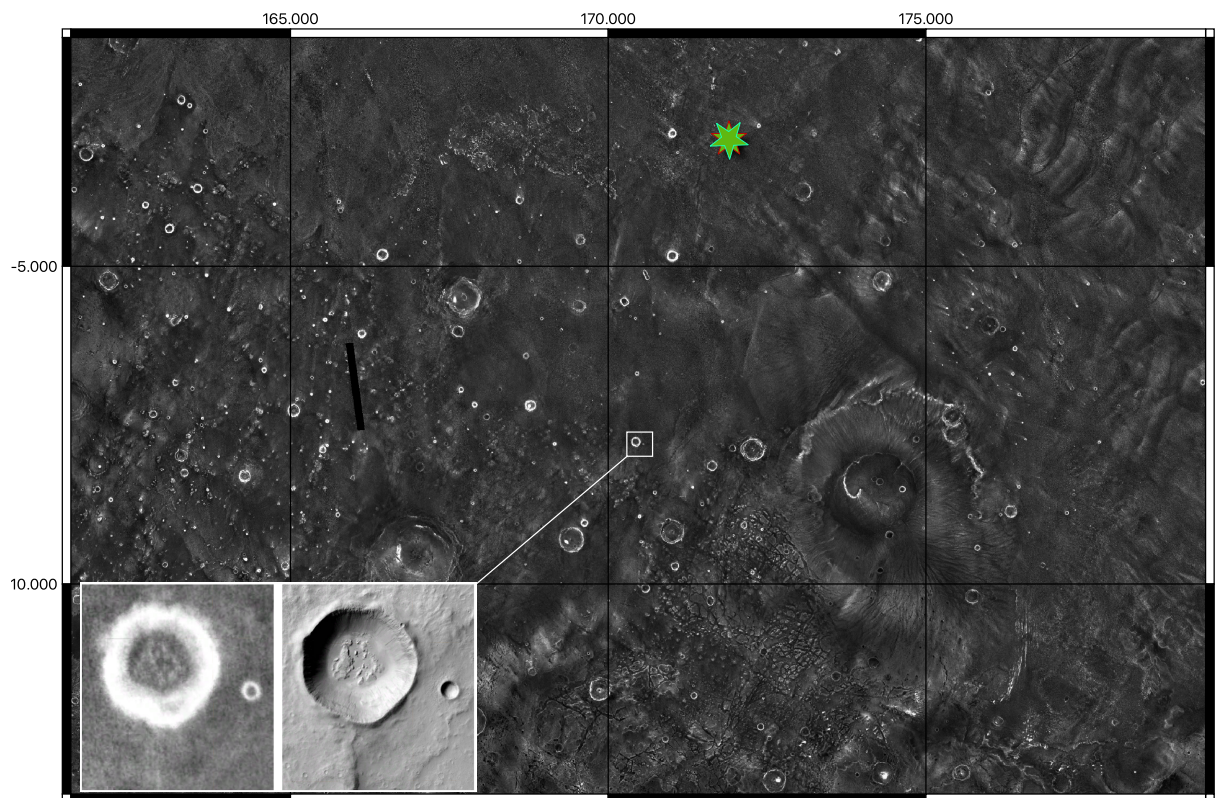


Figure S3: Apparent thermal inertial map derived from THEMIS-IR over the region of interest provided by the USGS. Green star is the epicentral location estimated from Kawamura et al. (2023). Inset shows a close-up on a crater presenting dust avalanches with thermal inertia and its visible counterpart from CTX.

Text S3. Note on triggering factors

Avalanche motion treated as a single-phase dry granular flow with Coulomb-type behaviour can be described by a two-dimensional Saint-Venant system. Hence, the transition between a static state and a flowing state is modelled by introducing a threshold allowing the material to flow. The friction forces $f(x, y, t)$ must satisfy

$$\|f(x, y, t)\| \leq \mu \rho g h, \quad (1)$$

where μ is the friction coefficient, ρ the density, g acceleration due to the gravity, and h the thickness. This has been shown to quantitatively capture debris and rock avalanche morphodynamics on Mars (Lucas; 2010; Lucas and Mangeney; 2007; Lucas et al.; 2011, 2014). Hence, this transition is sensitive to ground acceleration or dust deposition. To evaluate the stability of a slope composed of Martian dust, taking into account the potential cohesion of dust due to electrostatic forces, one can use the Coulomb failure criterion

$$\tau = c + \sigma_n \tan(\phi), \quad (2)$$

where: τ is the shear stress, c is the cohesion of the material, σ is the normal stress, and ϕ is the angle of internal friction (where $\mu = \tan(\phi)$). The normal stress on a slope is calculated as:

$$\sigma_n = \rho g h \cos^2(\theta), \quad (3)$$

where ρ is the density of the material, g is the acceleration due to the gravity, h is the depth of the material, and θ is the slope angle.

• Triggering by dust deposition

The additional shear stress $\delta\tau$ due to an additional height δh of deposition is estimated by:

$$\delta\tau = \rho g \delta h \sin(\theta) \cos(\theta) \quad (4)$$

By rearranging the aforementioned equations, the additional deposit height necessary for slope failure, denoted as δh , can be calculated. One can perform a parametric exploration accounting for the following parameter ranges estimated from soil mechanics experiments recently performed with HP³ on InSight Spohn et al. (2022a,b): initial dust thickness $h = \{10 \text{ cm}, 2\text{m}\}$, slope angle $\theta = 30^\circ$, friction angle $\phi = \{12^\circ, 25^\circ, 35^\circ\}$ and cohesion $c = \{0, 12\}$ (kPa). The additional dust height δh required to trigger failure ranges from millimetric to metric scales as illustrated in the Fig. S4. These ranges can be compared to the typical dust deposition rates observed on the ground from both rovers and landers. As a matter of fact, dust deposition of a few particles radius per 100 sols are observed at the MER rover locations (Kinch et al.; 2007). By considering the 140 sols between the closest image pair ($L_s = \{80; 220\}$) and the typical grain size radii discussed by Kinch et al. (2007), would lead to 140 sols x 3 radii/100 sols x $1.5 \mu\text{m} = 6.30 \mu\text{m}$, which is 3 folds smaller than the lower bound discussed previously. Accounting for larger particle radii ($r=60 \mu\text{m}$) as it was assessed around the InSight landing site (Chen-Chen et al.; 2023), the dust accumulation would be around $250 \mu\text{m}$ over the 140 sols period, which is comparable to the dust settling rate which was recorded to be $1 \mu\text{m}/\text{sols}$ at Phoenix landing site (Drube et al.; 2010). Still, such extreme values of dust rate would be insufficient.

The dust rate at the S1222a location can be estimated from GCMs results, by dividing the total dust deposit over the 140 sols period by the density of the material. Considering a of 1600 kg.m^{-3} and a typical mean dust deposition of $0.5 \times 10^{-9} \text{ kg.m}^{-2}.\text{s}^{-1}$ (Figure S5), the deposit accumulated is of about $7 \mu\text{m}$, which in agreement to MER's location observations as shown in Kinch et al. (2007). Additionally, pre-event images display wind streaks oriented northward, associated with small impact craters. However, post-event images do not show any changes, casting doubt on the wind's ability to transport dust within the observed time span (Fig S6). Predictions from GCM indicate surface wind speed below 3 m.s^{-1} if we except slope winds over Apollinaris Mons (Figure S7). Finally, the orientation of the slopes on which avalanches are observed, whether in images before or after event S1222a, show the same distribution as that of steep slopes ($>10^\circ$), which allows us to rule out, once again, any connection with the action of the wind (Fig. S8).

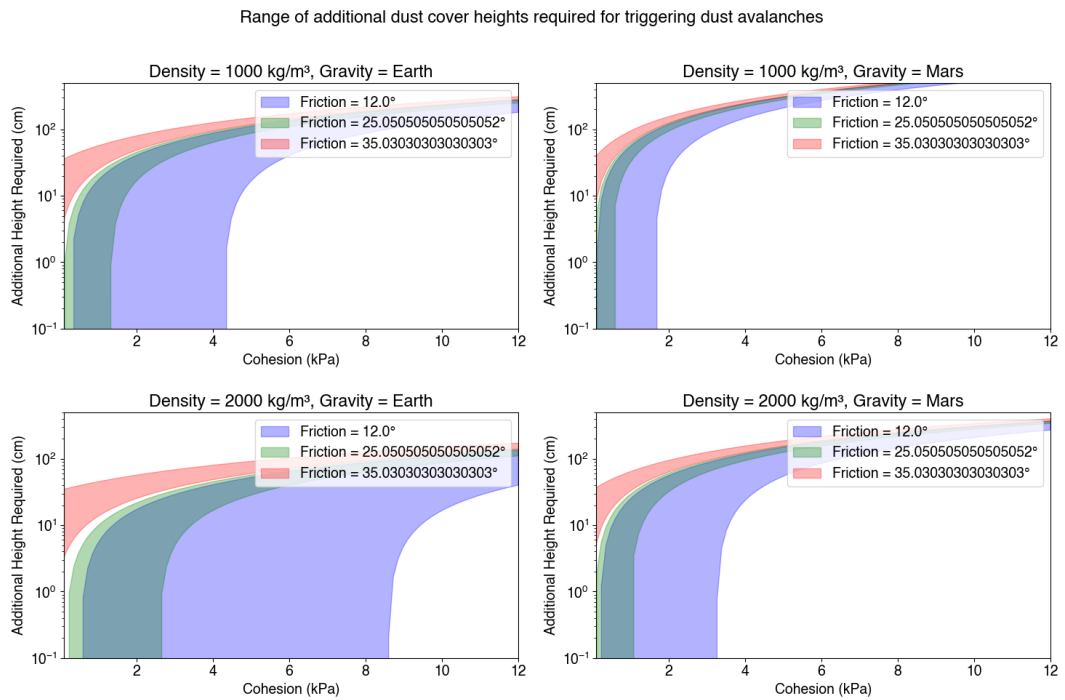


Figure S4: Estimation of the required additional dust heights for reaching slope failure under various conditions. The bounds for each computation are corresponding to an initial dust thickness ranging from 10 cm (lower bounds) up to 2 meters (upper bounds) and a slope angle of 30° .

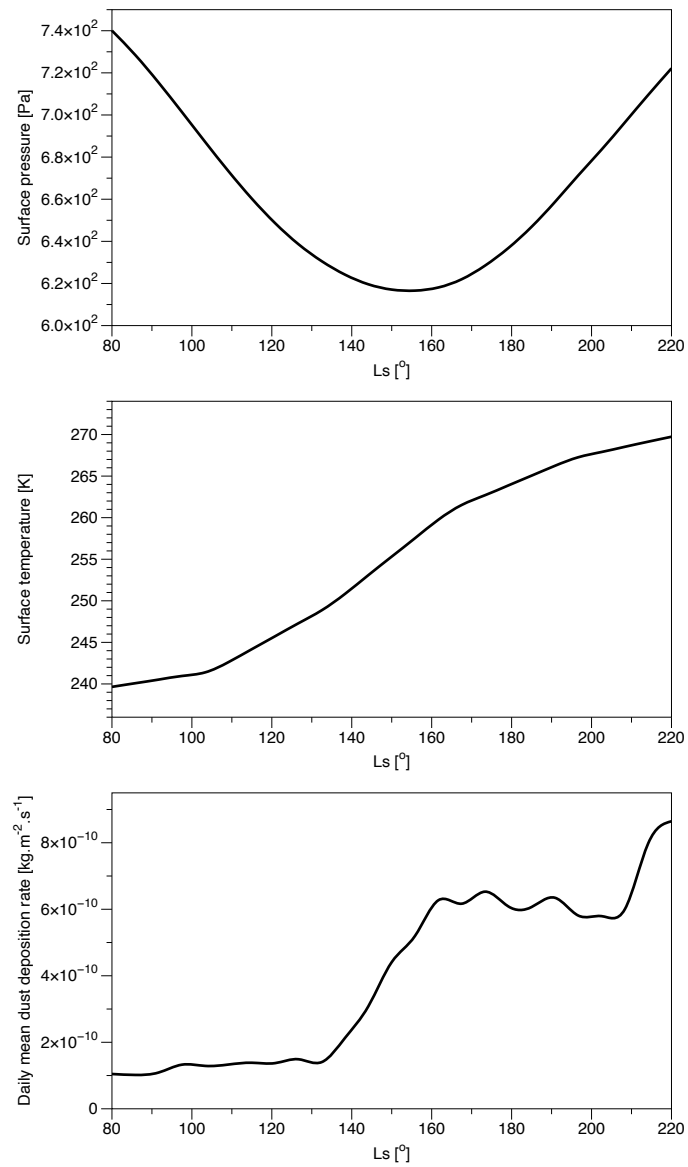


Figure S5: LMD GCM predictions for (top) Surface atmospheric pressure at the S1222a area computed at 2pm, from Ls ranging from 80 to 220; (center) Surface temperature; (bottom) Daily mean dust deposition rate for the same period. Plots generated from the Mars Climate Database (c) LMD/LATMOS/OU/IAA/ESA/CNES.

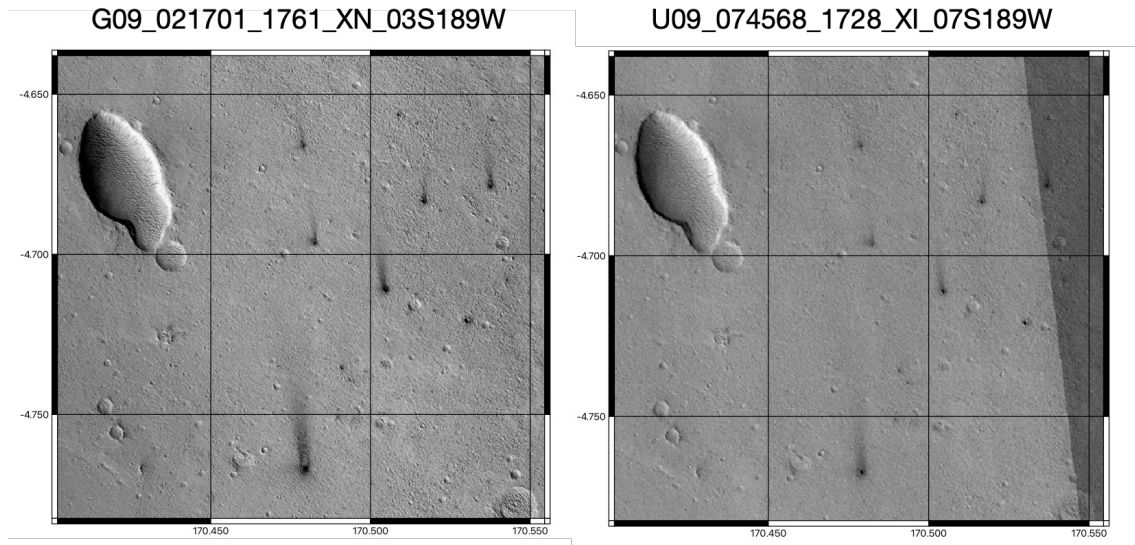


Figure S6: Wind streaks as observed from both pre- and post- S1222a event images.

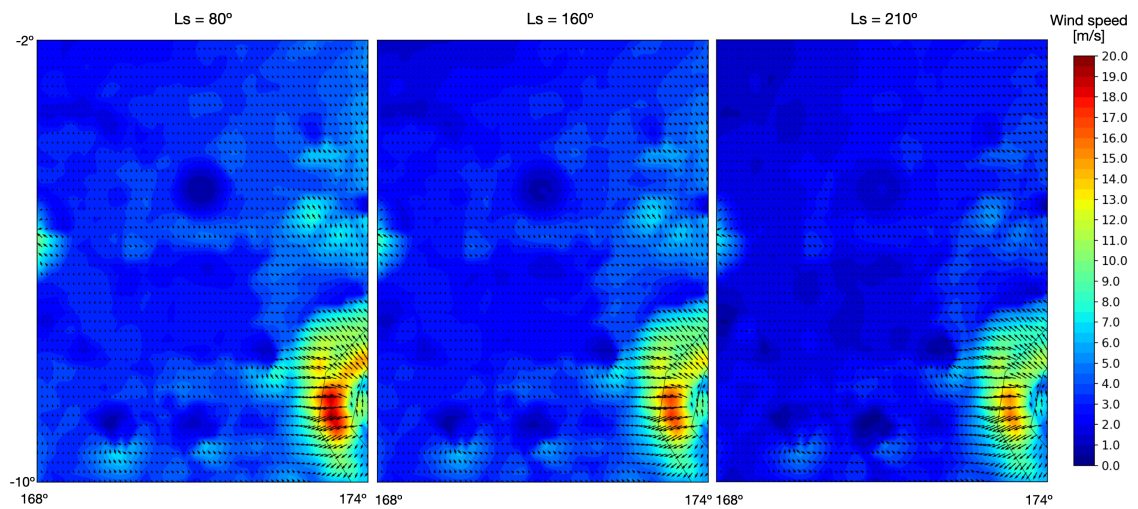


Figure S7: Surface wind speed predicted from GCM at different Ls. Plots generated from the Mars Climate Database (c) LMD/LATMOS/OU/IAA/ESA/CNES.

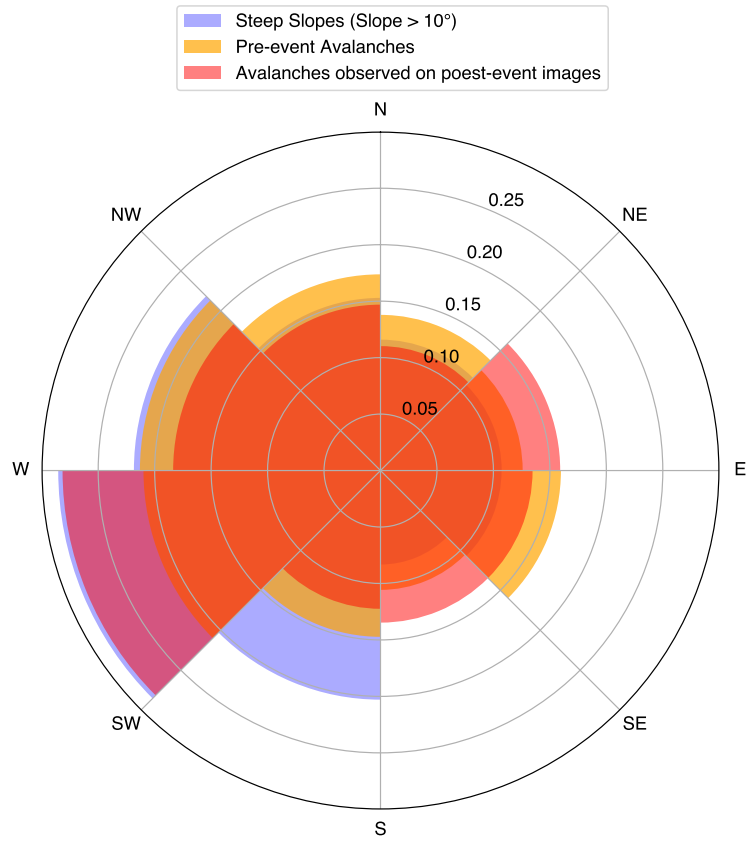


Figure S8: Distribution of steep slopes orientation ($>10^\circ$) from MOLA data at 128ppd over the region of the S1222a event, covered by figure S2 (in blue). Orientation at avalanche locations from pre-event images (orange) and post-event images (red).

- **Triggering by atmospheric pressure variation**

In order to evaluate the atmospheric pressure variation required to initiate slope failure, we need to focus on the change in shear stress. The pressure variation, in this context, is essentially the increase in shear stress needed to reach the failure point. To find the pressure variation required for failure, one needs to calculate the difference between the current shear stress due to the weight of the material and the shear strength (given by the Coulomb failure criterion). This difference represents the additional shear stress required to reach the failure condition. For the specified parameters (cohesion of 1000 Pa, friction angle of 30 degrees, density of 1600 kg/m³, height of 1 meter, slope angle of 30 degrees, and Martian gravity), the calculated pressure variation (additional shear stress) required to initiate slope failure is approximately 1000 Pascals. In comparison, the typical pressure variations due to turbulence observed at the InSight landing site are of about a few 10's of Pa, which is two folds smaller than the required pressure variations.

- **Triggering by ground acceleration**

To evaluate how ground acceleration from seismic activity, could contribute to reaching the slope failure condition, we need to consider the additional shear stress induced by this acceleration. One can approach this by considering the pseudostatic analysis, where the seismic force is simplified as a static force acting on the slope. The additional shear stress ($\delta\tau$) due to ground acceleration (a) can be estimated using the formula:

$$\delta\tau = \rho ah \sin(\theta), \quad (5)$$

where a is the horizontal ground acceleration. The total shear stress acting on a slope is the cumulative effect of the inherent shear stress, which is a consequence of gravitational forces, and the additional shear stress induced by ground acceleration. A slope is prone to failure when this combined shear stress surpasses the material's shear strength, as defined by the Coulomb failure criterion. Continuing with the same parameters as before — cohesion (c) at 1000 Pa, internal friction angle at 30 degrees, density at 1600 kg.m⁻³, and a slope angle of 30 degrees — we consider a hypothetical ground acceleration of 0.5 m.s⁻², which is 15% of Martian gravity (A typical M_w 5 on Earth leads to 10% of terrestrial gravity, (e.g., Sandron et al.; 2019)). Under these conditions, an initial material thickness of 3 meters results in the total shear stress beginning to surpass the shear strength. This indicates a condition likely to lead to slope failure.

A key factor influencing the outcome in terms of both total shear stress and shear strength is the initial height of the material on the slope. Within our model's framework, the gravitational shear stress and the extra shear stress from ground acceleration are both directly proportional to the material's height. Consequently, an increase in height leads to a corresponding rise in both types of stress. However, the rates at which they increase may vary. This variance plays a crucial role in determining how changes in height influence the probability of slope failure. This aspect can be related to the fact the thermal properties, as shown in the main text, seems to control the increase of the avalanche rate.

The ground acceleration associated with an earthquake is generally evaluated through the PGA (Peak Ground Acceleration), the maximum amplitude recorded during an earthquake. On the zeroth-order, this value will depend on the epicentral distance. Following Gomberg et al. (2006); Gomberg and Felzer (2008), we can relate the ground motion G with epicentral distance Δ through this simple relation:

$$PGA(\Delta) = \frac{K}{(\alpha + \Delta)^2}, \quad (6)$$

where K and α are empirical parameters (Gomberg and Felzer; 2008). Nonetheless, as on Earth, avalanches or rockfalls occur in response to a combination and cumulative forcings acting at different time scales including gravity, weathering and chemical effects, thermal, meteorological, seismic or volcanic activities (e.g., Tatar; 2010).

Text S4. Note on the inversion method and uncertainties

Following Mosegaard and Tarantola (1995), we can use inverse problem method to estimate what is the epicentral location that best explain the avalanche rate derived from orbital imagery.

As the "direct problem" consisting in predicting the d-values that we should observe when we make observations on a given system, such system can be described by a vector \mathbf{m} of parameters, such as $\mathbf{m} = \{m_1, m_2, \dots, m_i\}$. We can define a probability density $\sigma(\mathbf{m})$ that combines the a priori $\rho(\mathbf{m})$ information with the information provided by the experimental measurements (the data vector) and the information provided by the physics of the problem (i.e., the model). Hence, $\sigma(\mathbf{m})$ is called the posterior information. It is the combination of all the information we have and reads:

$$\sigma(\mathbf{m}) = k\rho(\mathbf{m})L(\mathbf{m}), \quad (7)$$

with k being a normalization constant (=1) and $L(\mathbf{m})$ the likelihood function accounting for a Laplacian experimental uncertainties, which reads:

$$L(\mathbf{m}) = \exp \left[- \sum_i \frac{\|G^i(\mathbf{m}) - d_{obs}^i\|}{\sigma_i} \right], \quad (8)$$

where $G^i(\mathbf{m})$ is the prediction by the model $G(\mathbf{m})$ of the i^{th} observation, d_{obs}^i is the i^{th} observation with its associated uncertainties σ_i . In this study, the model $G(\mathbf{m})$ is provided after Livio and Ferrario (2020) which relates the avalanche (or landslides in their paper) distribution with the epicentral distance Δ :

$$G(\mathbf{m}) = N_{ava} = a \exp \left[- \left(\frac{\Delta - b}{c} \right)^2 \right], \quad (9)$$

where N_{ava} is the avalanches number triggered by the seismic event, where $\mathbf{m} = \{a, b, c\}$, with a the peak amplitude of the distribution, b the distribution peak distance to the epicenter, and c the distribution width.

Hence, we randomly explore the longitude-latitude space (Lon \in [166,175] and Lat \in [-10,-1]) over 1 million runs. For each run, compute the epicentral distance for each avalanche's area that meet both conditions (Δt ; 1.5 MYear and $\Gamma^* < 450$). Then, we fit the equation 9 on the observed N_{ava} vs Δ (expressed in euclidean distances and accounting for Mars flattening) using a non-linear least squares method. Finally, we compute the maximum likelihood function from equation 8 which accounts for a Laplacian distribution of uncertainties on the avalanche number.

The uncertainties on the avalanche rate q is computed after Aharonson et al. (2003), which reads:

$$\sigma = \left\langle \left(q - \langle q \rangle \right)^{1/2} \right\rangle^2 = \frac{\langle q \rangle}{\sqrt{1 + \sum_i \Delta n_i}}, \quad (10)$$

with $\langle q \rangle$ being the expectation value of q , which reads:

$$\langle q \rangle = \frac{1 + \sum \Delta n_i}{\sum_i n_i \Delta t_i}. \quad (11)$$

References

- Aharonson, O., Schorghofer, N. and Gerstell, M. F. (2003). Slope streak formation and dust deposition rates on Mars: Martian slope streak formation rates, *Journal of Geophysical Research: Planets* **108**(E12).
- Balme, M. R., Whelley, P. L. and Greeley, R. (2003). Mars: Dust devil track survey in argyre planitia and hellas basin, *Journal of Geophysical Research: Planets* **108**(E8).
- Battalio, M. and Wang, H. (2021). The Mars Dust Activity Database (MDAD): A comprehensive statistical study of dust storm sequences, *Icarus* **354**: 114059.
- Bergonio, J. R., Rottas, K. M. and Schorghofer, N. (2013). Properties of martian slope streak populations, *Icarus* **225**(1): 194–199.
- Chen-Chen, H., Pérez-Hoyos, S., Sánchez-Lavega, A. and Peralta, J. (2023). Characterisation of deposited dust particles on mars insight lander instrument context camera (icc) lens, *Icarus* **392**: 115393.
- Daubar, I., Dundas, C., Byrne, S., Geissler, P., Bart, G., McEwen, A., Russell, P., Chojnacki, M. and Golombek, M. (2016). Changes in blast zone albedo patterns around new martian impact craters, *Icarus* **267**: 86–105.
- Drube, L., Leer, K., Goetz, W., Gunnlaugsson, H. P., Haspang, M. P., Lauritsen, N., Madsen, M. B., Sørensen, L. K. D., Ellehoj, M. D., Lemmon, M. T., Morris, R. V., Blaney, D., Reynolds, R. O. and Smith, P. H. (2010). Magnetic and optical properties of airborne dust and settling rates of dust at the phoenix landing site, *Journal of Geophysical Research: Planets* **115**(E5).
- Geissler, P. E., Sullivan, R., Golombek, M., Johnson, J. R., Herkenhoff, K., Bridges, N., Vaughan, A., Maki, J., Parker, T. and Bell, J. (2010). Gone with the wind: Eolian erasure of the mars rover tracks, *Journal of Geophysical Research: Planets* **115**(E7).
- Gomberg, J. and Felzer, K. (2008). A model of earthquake triggering probabilities and application to dynamic deformations constrained by ground motion observations, *Journal of Geophysical Research: Solid Earth* **113**(B10).
- Gomberg, J., Felzer, K. R. and Brodsky, E. E. (2006). Earthquake dynamic triggering and ground motion scaling.
- Kawamura, T., Clinton, J., Zenhäusern, G., Ceylan, S., Horleston, A., Dahmen, N., Duran, C., Kim, D., Plasman, M., Stähler, S., Euchner, F., Charalambous, C., Giardini, D., Davis, P., Sainton, G., Lognonné, P., Panning, M. and Banerdt, W. (2023). S1222a - the largest Marsquake detected by InSight, *Geophysical Research Letters* .

- Kinch, K. M., Sohl-Dickstein, J., Bell III, J. F., Johnson, J. R., Goetz, W. and Landis, G. A. (2007). Dust deposition on the mars exploration rover panoramic camera (pancam) calibration targets, *Journal of Geophysical Research: Planets* **112**(E6).
- Livio, F. and Ferrario, M. F. (2020). Assessment of attenuation regressions for earthquake-triggered landslides in the italian apennines: insights from recent and historical events, *Landslides* **17**(12): 2825–2836.
- Lucas, A. (2010). *Dynamique des instabilités gravitaires par modélisation et télédétection: Applications aux exemples martiens*, Theses, Institut de physique du globe de paris - IPGP.
URL: <https://tel.archives-ouvertes.fr/tel-00503212>
- Lucas, A. and Mangeney, A. (2007). Mobility and topographic effects for large valles marineris landslides on mars, *Geophysical Research Letters* **34**(10).
- Lucas, A., Mangeney, A. and Ampuero, J. P. (2014). Frictional velocity-weakening in landslides on earth and on other planetary bodies, *Nature Communications* **5**(1): 3417.
- Lucas, A., Mangeney, A., Mège, D. and Bouchut, F. (2011). Influence of the scar geometry on landslide dynamics and deposits: Application to martian landslides, *Journal of Geophysical Research: Planets* **116**(E10).
- Mosegaard, K. and Tarantola, A. (1995). Monte carlo sampling of solutions to inverse problems, *Journal of Geophysical Research: Solid Earth* **100**(B7): 12431–12447.
- Neukum, G. and Jaumann, R. (2004). The high resolution stereo camera of mars express, *ESA Special Publication* **1240**: 1–19.
- Perrin, C., Rodriguez, S., Jacob, A., Lucas, A., Spiga, A., Murdoch, N., Lorenz, R., Daubar, I. J., Pan, L., Kawamura, T., Lognonné, P., Banfield, D., Banks, M. E., Garcia, R. F., Newman, C. E., Ohja, L., Widmer-Schmidrig, R., McEwen, A. S. and Banerdt, W. B. (2020). Monitoring of dust devil tracks around the insight landing site, mars, and comparison with in situ atmospheric data, *Geophysical Research Letters* **47**(10): e2020GL087234.
- Sandron, D., Santulin, M., Tamaro, A., Orzi, C., Benedetti, G., Castellaro, S., Romeo, R., Rebez, A., Grimaz, S., Malisan, P., Guadagnini, G., Sciascia, F. and Slejko, D. (2019). Seismic parameter design assessment for the kribi deep seaport in cameroon, *Bulletin of Earthquake Engineering* **17**.
- Schorghofer, N., Aharonson, O., Gerstell, M. and Tatsumi, L. (2007). Three decades of slope streak activity on mars, *Icarus* **191**(1): 132–140.
- Smith, D. E., Zuber, M. T., Frey, H. V., Garvin, J. B., Head, J. W., Muhleman, D. O., Pettengill, G. H., Phillips, R. J., Solomon, S. C., Zwally, H. J., Banerdt, W. B., Duxbury, T. C., Golombek, M. P., Lemoine, F. G., Neumann, G. A., Rowlands, D. D., Aharonson, O., Ford, P. G., Ivanov, A. B., Johnson, C. L., McGovern, P. J., Abshire, J. B., Afzal, R. S. and Sun, X. (2001). Mars orbiter laser altimeter: Experiment summary after the first year of global mapping of mars, *Journal of Geophysical Research: Planets* **106**(E10): 23689–23722.

- Spohn, T., Hudson, T. L., Marteau, E., Golombek, M., Grott, M., Wippermann, T., Ali, K. S., Schmelzbach, C., Kedar, S., Hurst, K., Trebi-Ollennu, A., Ansan, V., Garvin, J., Knollenberg, J., Müller, N., Piqueux, S., Lichtenheldt, R., Krause, C., Fantinati, C., Brinkman, N., Sollberger, D., Delage, P., Vrettos, C., Reershemius, S., Wisniewski, L., Grygorczuk, J., Robertsson, J., Edme, P., Andersson, F., Krömer, O., Lognonné, P., Giardini, D., Smrekar, S. E. and Banerdt, W. B. (2022b). The insight HP³ penetrator (mole) on mars: Soil properties derived from the penetration attempts and related activities, *Space Science Reviews* **218**(8): 72.
- Spohn, T., Hudson, T., Witte, L., Wippermann, T., Wisniewski, L., Kedziora, B., Vrettos, C., Lorenz, R., Golombek, M., Lichtenheldt, R., Grott, M., Knollenberg, J., Krause, C., Fantinati, C., Nagihara, S. and Grygorczuk, J. (2022a). The InSight-HP³ mole on Mars: Lessons learned from attempts to penetrate to depth in the martian soil, *Advances in Space Research* **69**.
- Sullivan, R., Thomas, P., Veverka, J., Malin, M. and Edgett, K. S. (2001). Mass movement slope streaks imaged by the mars orbiter camera, *Journal of Geophysical Research: Planets* **106**(E10): 23607–23633.
- Tatard, L. (2010). *Statistical analysis of triggered landslides : implications for earthquake and weather controls*, PhD thesis, University of Canterbury and Université de Grenoble.
- Verba, C. A., Geissler, P. E., Titus, T. N. and Waller, D. (2010). Observations from the high resolution imaging science experiment (hirise): Martian dust devils in gusev and russell craters, *Journal of Geophysical Research: Planets* **115**(E9).